PLL Synchronization Transient Stability Analysis of a Weak-Grid Connected VSC During Asymmetric Faults

Zhi Wang, Li Guo, *Member, IEEE*, Xialin Li, *Member, IEEE*, Xiulan Pang, Xiaofeng Li, Xu Zhou, and Chengshan Wang, *Senior Member, IEEE*

***Abstract*—During asymmetric faults, the coupling between positive and negative (PN) sequences significantly affects the phase-locked-loop (PLL) synchronization transient stability (PSTS) of a weak-grid connected voltage source converter (WG-VSC). However, little literature is on analyzing the PSTS while considering PN sequence coupling. This article has analyzed the PSTS of the WG-VSC system considering PN sequence coupling under asymmetric faults for the first time. First, the Takagi–Sugeno method is adopted to construct the largest estimated domain of attraction (LEDA) at an equilibrium point of the system during asymmetric faults. This LEDA enables quantitative analysis of PLL synchronization transient instability phenomena. Furthermore, from the point of view of ensuring the PSTS, the feasible region of PN currents (FR-PNC) of the system during asymmetric faults has been obtained. In addition, an algorithm is proposed to visualize this 4-D FR-PNC in 2-D space. Finally, the theoretical analysis is validated by time domain experiments conducted on the RT-Box hardware-in-the-loop experimental platform.**

***Index Terms*—Asymmetric faults, feasible region of positive and negative (PN) currents (PNC), phase-locked-loop (PLL) synchronization transient stability (PSTS), sequence coupling.**

I. Introduction

With a high proportion of renewable energy generation replacing traditional synchronous generators, the short-circuit capacity of the power grid has been gradually weakened. As a result, power electronic interface sources, dominated by voltage source converters (VSCs), are increasingly facing weak grid-connected operating scenarios [1]. Numerous studies indicate that weak-grid connected VSC (WG-VSC) are at risk of phase-locked-loop (PLL) synchronization transient instability under significant disturbances, such as faults [2]. Hence, there is a need to investigate the PLL synchronization transient stability (PSTS) issue of the systems during grid faults.

Previously, most studies focused on investigating the PSTS issue of the system under symmetric fault. For example, with the equal-area criterion (EAC), the PSTS mechanism of the system has been revealed in [3] and [4]. Hu et al. [5] highlighted that grid faults can lead to insufficient damping or even negative damping, which will deteriorate the PSTS of the system. The EAC cannot consider the impact of negative damping. Thus, the phase trajectory method [6], inverse trajectory method [7], and Lyapunov direct method [8], [9] have been applied to study the PSTS of the system, respectively. Some studies have investigated the effect of PLL frequency limiting [10], [11] and the interaction between the current control and PLL control [12] on the PSTS of the system. In [10], the EAC was employed to study the PSTS of the system considering sequential switching schemes. Recent works extended this research to grid-tied multiconverter systems [14], [15]. The above studies primarily focus on symmetrical faults. Note that the PSTS under asymmetric faults is also important [16]. However, the models and analysis methods proposed in the above studies are insufficient to address PSTS issues under asymmetric faults [17], which is the primary motivation of this article.

Currently, only a few pieces of literature, such as [6] and [20], have analyzed the PSTS of the system under asymmetric faults while ignoring the effects of positive and negative (PN) sequence coupling. In [6], by neglecting the effect of negative-sequence (NS) networks, the positive-sequence (PS) PSTS of the system in asymmetric faults was studied with the phase trajectory method. Similarly, in [18], NS synchronization control dynamics were ignored, and the NS phase angle was assumed to equal the inverse of the PS phase angle. Nevertheless, Ahmed et al. [19] emphasized that for achieving precise NS current control, the NS phase angle must be tracked using NS PLL. Li et al. [20] point out that the effect of PN sequence coupling on the PSTS of the system can be neglected when the fault location is far from the point of common coupling (PCC). Furthermore, an analytical transient stability criterion is proposed in [20] based on energy conversion. However, the effect of PN sequence coupling on the PSTS of the system cannot be neglected in certain scenarios where the fault location is close

Manuscript received 13 June 2023; revised 18 September 2023 and 21 October 2023; accepted 11 November 2023. Date of publication 17 November 2023; date of current version 22 December 2023. This work was supported in part by the National Key R&D Program of China under Project 2023YFB2406700, in part by the Academician Innovation Platform Project of Hainan Province under Project YSPTZX202305, and in part by the National Nature Science Foundation of China under Project 51977142. Recommended for publication by Associate Editor S. Golestan. *(Corresponding author: Xialin Li.)*

Zhi Wang, Li Guo, Xialin Li, Xu Zhou, and Chengshan Wang are with the Key Laboratory of Smart Grid of Ministry of Education, Tianjin University, Tianjin 300072, China (e-mail: 2020234352@tju.edu.cn; liguo@tju.edu.cn; xialinlee@tju.edu.cn; zhouxu@tju.edu.cn; cswang@tju.edu.cn).

Xiulan Pang and Xiaofeng Li are with the SPIC Qinghai Photovoltaic Industry Innovation Center, Xining 810000, China (e-mail: pangxiulan@spic.com.cn; hefengqin@spic.com.cn).

Color versions of one or more figures in this article are available at https://doi.org/10.1109/TPEL.2023.3333808.

Digital Object Identifier 10.1109/TPEL.2023.3333808

to PCC, which will be verified in the theoretical analysis and simulation results in this article.

Few studies have investigated the effect of PN sequence coupling on the PSTS of the system under asymmetric faults. However, the relevant studies have primarily focused on the presence of equilibrium points (EPs) and the local stability analysis around EPs (small-signal stability analysis), with little consideration of transient dynamics. In [21], [22], and [23], the effect of PN sequence coupling on the existence of EPs in WG-VSC systems under asymmetric faults has been analyzed. At the precondition of existing EPs, the local stability around the EPs of the system has been investigated with complex impedance analysis and transfer function theory in [24] and [25]. Notably, literature [21], [22], [23], [24], and [25] hardly involved transient process analysis. Thus, the research in [21], [22], [23], [24], and [25] cannot address the transient stability issue, specifically whether the system can stably reach the locally stable EP of fault-on from the EP of prefault under asymmetric faults. This article mainly focuses on addressing this issue.

The PN sequence current injection strategies of the system have a considerable impact on the PSTS of the system during asymmetric fault ride-through. Thus, the feasible region of positive and negative currents (FR-PNC) for ensuring the PSTS is particularly valuable for current reference design during asymmetric fault. The FR-PNC was initially constructed in [23] to ensure the existence of EPs. However, it does not consider the PSTS constraint. Thus, even if the injection currents fall within the FR-PNC constructed in [23], PSTS may still lose, which had been verified in [20]. The concept of FR-PNC from the perspective of ensuring PSTS under asymmetric faults was first introduced in [20]. However, the influence of PN sequence coupling was not considered in [20], which may affect PSTS significantly, as validated in this article.

The contributions of this article are summarized as follows.

1) Considering PN sequence coupling, the PSTS of the system during asymmetric faults is studied for the first time. The Takagi–Sugeno (TS) method is employed to obtain the largest estimated domain of attraction (LEDA) at an available EP of the system. With the LEDA, we provide a theoretical explanation for the phenomena of transient instability. The phenomenon refers to the system cannot stably reach a new available EP during asymmetric faults from the prefault state.
2) For the first time, the FR-PNC of WG-VSC considering PN sequence coupling is built with the perspective of ensuring PSTS during asymmetric faults. Then, an algorithm is proposed to visualize this 4-D FR-PNC in 2-D space for better display.

The rest of this article is organized as follows. In Section II, a fourth-order model for PSTS analysis is developed and validated. Section III analyzes the PSTS of the system considering PN sequence coupling. Then, the FR-PNC of the system is built, and an algorithm to visualize this 4-D FR-PNC in 2-D space is proposed in Section IV. Additionally, experimental results are provided to validate the theoretical analysis. Finally, Section V concludes this article.

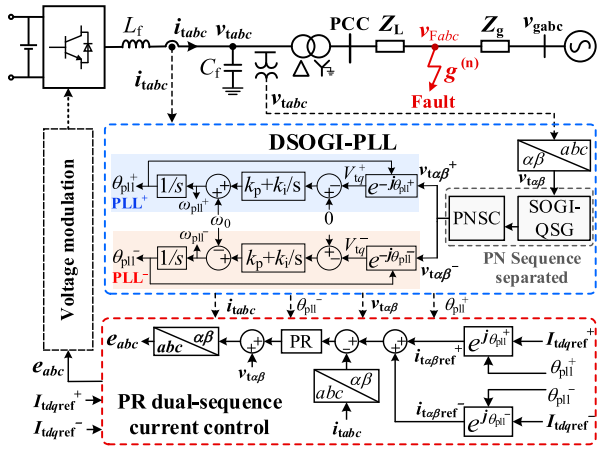

Fig. 1. Topology of the WG-VSC system.

II. WG-VSC System and Its Reduced-Order Model

A. System Description

The topology of the system is presented in Fig. 1, VSC is connected to the weak grid through a Delta-wye (Dy) grounded step-up transformer. The impedance of the transformer is much less than the line impedance, thus the transformer is considered an ideal transformer in this article. In Fig. 1, v_{tabc}, v_{Fabc}, and v_{gabc} are the *abc* three-phase components of low-voltage-side PCC voltage, fault point voltage, and infinite-bus voltage, respectively. i_{tabc} denotes the *abc* three-phase component of the current injected by VSC into the grid. The equivalent impedances from PCC to fault location and from fault location to infinite bus are denoted as $\mathbf{Z_L}$ and $\mathbf{Z_g}$, respectively. Notably, different asymmetric fault types are denoted by $g^{(\mathrm{n})}$, where $g^{(1)}$, $g^{(2)}$, and $g^{(3)}$ denote single line-to-ground (SLG), double line-to-ground (DLG), and line-to-line (LL) faults, respectively.

The control strategy of VSC comprises dual second-order generalized integrator-based PLL (DSOGI-PLL) and proportional resonant (PR) dual-sequence current control in stationary reference frames, as depicted in Fig. 1. During asymmetric faults, the second-order generalized integrator-quadrature signals generator (SOGI-QSG) and positive/negative sequence calculation extract the PS and NS PCC voltages. Then, the PLL$^+$ and PLL$^-$ track the phase of both the PS and NS PCC voltages, respectively. It outputs the angular frequencies $\omega_{\mathrm{pll}}^{+}\mathrm{and}\omega_{\mathrm{pll}}^{-}$ and phase angles $\theta_{\mathrm{pll}}^{+}\mathrm{and}\theta_{\mathrm{pll}}^{-}$ of the PS and NS PCC voltages.

The PR current control regulates the converter-side currents, enabling the VSC dual-sequence injection current to follow the PS and NS current reference values $I_{\mathrm{tdref}}^{+}\mathrm{and}I_{\mathrm{tqref}}^{+}$ and $I_{\mathrm{tdref}}^{-}\mathrm{and}I_{\mathrm{tqref}}^{-}$. During normal operation, the PS current references I_{tdref}^{+} and I_{tqref}^{+} are determined by the active power loop and reactive power loop, respectively. When the WG-VSC system is exposed to asymmetric grid faults, the PS and NS sequence current references are directly specified by the asymmetric fault ride-through control strategy [3], [4], [5], [6], [7], [8], [9], [10], [11], [12], [13], [21], [22], [23], as illustrated in Fig. 2. In Fig. 2, P and Q are the active and reactive output power of VSC, P_{ref} and Q_{ref} are the reference values of prefault active and

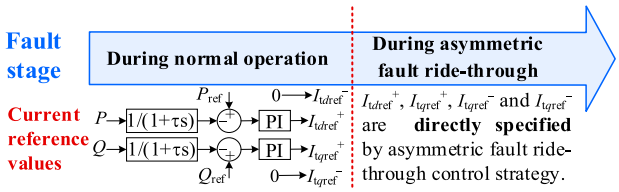

Fig. 2. PS and NS sequence current references.

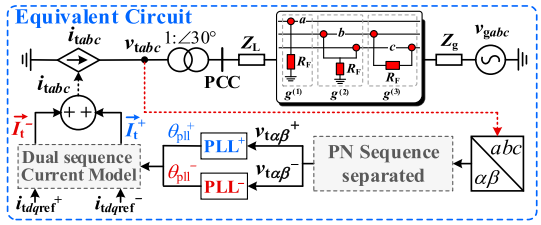

Fig. 3. Equivalent circuit diagram of the system.

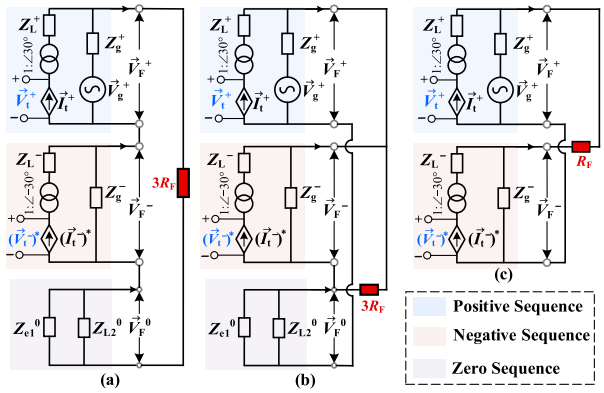

Fig. 4. Sequence network of the system under asymmetric fault. (a) SLG fault. (b) DLG fault. (c) LL fault.

reactive power, respectively, and τ represents the low-pass filter coefficient. Further detailed descriptions of the VSC control can be found in [20] and [26].

As shown in Fig. 1, the high-voltage-side zero-sequence circuit is closed by the grounded neutral point. However, the low-voltage-side zero-sequence circuit is open. Thus, the voltages and currents of VSC, denoted as $x_{\rm abc}$, contain only PS and NS components.

The PS and NS rotating vectors of $x_{\rm abc}$ are denoted as $\vec{\boldsymbol{X}}^+$ and $\vec{\boldsymbol{X}}^-$, respectively, and then $x_{\rm abc}$ can be expressed as

$$x_{\rm abc} = \vec{\boldsymbol{X}}^+ + \vec{\boldsymbol{X}}^- = X^+ e^{j\theta^+} + X^- e^{j\theta^-} \tag{1}$$

where X^+ and X^- and θ^+ and θ^- are the amplitude and phase angle of the PS and NS rotating vectors, respectively. Note that $\theta^+ = \omega^+ t + \varphi^+$ and $\theta^- = \omega^- t + \varphi^-$ are time-variant, which contains the "rotational" attribute. ω^+ and ω^- and φ^+ and φ^- are the rotational angular frequencies and initial phase angles of the PS and NS vectors, respectively.

The vector diagram of $\vec{\boldsymbol{X}}^+$ and $\vec{\boldsymbol{X}}^-$ is shown in Fig. 20 (see Appendix A). As can be seen from Fig. 20, the transformation relations of the PS and NS vectors in the d^+q^+ and d^-q^- rotating coordinate systems are shown, respectively, in the following equations:

$$\vec{\boldsymbol{X}}^+ = \left(\boldsymbol{X}_{\boldsymbol{dq}}^+\right)^* e^{j\theta_{\rm pll}^+} = \left(X_d^+ - jX_q^+\right) e^{j\theta_{\rm pll}^+} \tag{2}$$

$$\vec{\boldsymbol{X}}^- = \left(\boldsymbol{X}_{\boldsymbol{dq}}^-\right)^* e^{j\theta_{\rm pll}^-} = \left(X_d^- - jX_q^-\right) e^{j\theta_{\rm pll}^-} \tag{3}$$

where $*$ denotes the complex conjugate operation, X_d^+ and X_q^+ and X_d^- and X_q^- are the projections of the PS and NS vectors on the d^+ and q^+ and d^- and q^- axes, respectively.

B. Fourth-Order Model of the System for PSTS Analysis

A fourth-order model for the system during asymmetric faults has been developed in this section. This article focuses on PSTS issues and several assumptions have been made, as previously considered in [20], [21], [22], and [23].

1) The transient dynamics of the *LC* filter and network have been neglected.
2) Dynamics of the SOGI-QSG have not been considered, and it is assumed that the DSOGI-PLL can instantaneously separate the PN sequence components of the PCC voltage.
3) It is assumed that I_{td}^+, I_{td}^-, I_{tq}^+, and I_{tq}^- can follow current reference values I_{tdref}^+, I_{tdref}^-, I_{tqref}^+, and I_{tqref}^- in real-time.
4) The effect of execution time and delay time has been disregarded.

Note that the above assumptions mainly affect high-frequency (hundreds to thousands Hz) dynamics of the system. However, this article focuses on the dynamics of the PLL synchronization timescale, which mainly affects the low-frequency (tens Hz) dynamics of the system. Thus, the above assumptions can be considered reasonable.

The equivalent circuit diagram of the system is developed with the above assumptions, as illustrated in Fig. 3. In Fig. 3, $R_{\rm F}$ is the ground resistance, and the dual sequence current model can be expressed as follows:

$$\begin{cases} \vec{\boldsymbol{I}}_{\mathbf{t}}^+ = (I_{\rm tdref}^+ - jI_{\rm tqref}^+) e^{j\theta_{\rm pll}^+} = I_{\rm t}^+ e^{j(-\theta_I^+ + \theta_{\rm pll}^+)} \\ \vec{\boldsymbol{I}}_{\mathbf{t}}^- = (I_{\rm tdref}^- - jI_{\rm tqref}^-) e^{j\theta_{\rm pll}^-} = I_{\rm t}^- e^{j(-\theta_I^- + \theta_{\rm pll}^-)} \end{cases} \tag{4}$$

where $I_{\rm t}^+ = \left\{\left(I_{\rm tdref}^+\right)^2 + \left(I_{\rm tqref}^+\right)^2\right\}^{1/2}$, $I_{\rm t}^- = \left\{\left(I_{\rm tdref}^-\right)^2 + \left(I_{\rm tqref}^-\right)^2\right\}^{1/2}$, $\theta_I^+ = \arctan\left(I_{\rm tqref}^+ / I_{\rm tdref}^+\right)$, and $\theta_I^- = \arctan\left(I_{\rm tqref}^- / I_{\rm tdref}^-\right)$.

The interconnection of the sequence network for different fault types can be obtained based on the boundary conditions under SLG, DLG, and LL, as shown in Fig. 4. The superscripts $+$, $-$, and 0 of impedance in Fig. 4 represent PS, NS, and zero sequence impedances, respectively.

Based on Fig. 4 and the superposition principle, the PS and NS voltages at PCC can be derived with the expressions given in the following equations:

$$\vec{\boldsymbol{V}}_{\mathbf{t}}^+ = \boldsymbol{K_1} \vec{\boldsymbol{V}}_{\mathbf{g}}^+ e^{-j\pi/6} + \boldsymbol{Z}_{\mathbf{e}}^+ \vec{\boldsymbol{I}}_{\mathbf{t}}^+ + \boldsymbol{Z}_{\mathbf{c}} \left(\vec{\boldsymbol{I}}_{\mathbf{t}}^-\right)^* e^{-j\pi/3} \tag{5}$$

$$\left(\vec{\boldsymbol{V}}_{\mathbf{t}}^-\right)^* = \boldsymbol{K_2} \vec{\boldsymbol{V}}_{\mathbf{g}}^+ e^{j\pi/6} + \boldsymbol{Z}_{\mathbf{e}}^- \left(\vec{\boldsymbol{I}}_{\mathbf{t}}^-\right)^* + \boldsymbol{Z}_{\mathbf{e}}^+ \vec{\boldsymbol{I}}_{\mathbf{t}}^+ e^{j\pi/3} \tag{6}$$

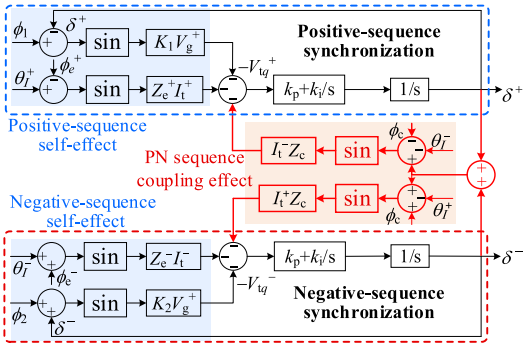

Fig. 5. Dynamic block diagram of the system during asymmetric faults.

where $\boldsymbol{Z}_{\mathbf{c}} = \boldsymbol{Z}_{\mathbf{g}}^{+}\boldsymbol{K}_2 = Z_{\mathrm{c}}\angle\phi_{\mathrm{c}}$, $\boldsymbol{Z}_{\mathbf{e}}^{+} = \boldsymbol{Z}_{\mathbf{g}}^{+}\ \boldsymbol{K}_1 + \boldsymbol{Z}_{\mathbf{L}}^{+} = Z_{\mathrm{e}}^{+}\angle\phi_{\mathrm{e}}^{+}$, $\boldsymbol{Z}_{\mathbf{e}}^{-} = \boldsymbol{Z}_{\mathbf{g}}^{-}\boldsymbol{K}_3 + \boldsymbol{Z}_{\mathbf{L}}^{-} = Z_{\mathrm{e}}^{-}\angle\phi_{\mathrm{e}}^{-}$, and $\boldsymbol{K}_i = K_i \angle \phi_i$ (i = 1,2,3). The expressions of $\boldsymbol{K}_i$ are given in Table IV of Appendix B.

Transforming (5) and (6) into the PLL^{+} and PLL^{-} reference coordinate systems, respectively, we can obtain the q-axis components of the PS and NS PCC voltages, denoted as V_{tq}^{+} and V_{tq}^{-}, and are expressed as follows:

$$\begin{aligned} V_{tq}^{+} &= K_1 V_{\mathrm{g}}^{+}\sin(\delta^{+}-\phi_1) + Z_{\mathrm{e}}^{+}I_{\mathrm{t}}^{+}\sin(\theta_I^{+}-\phi_{\mathrm{e}}^{+}) \\ &\quad + Z_{\mathrm{c}}I_{\mathrm{t}}^{-}\sin(\delta^{+}+\delta^{-}-\phi_{\mathrm{c}}-\theta_I^{-}) \end{aligned} \tag{7}$$

$$\begin{aligned} V_{tq}^{-} &= K_2 V_{\mathrm{g}}^{+}\sin(\delta^{-}+\phi_2) + Z_{\mathrm{e}}^{-}I_{\mathrm{t}}^{-}\sin(\phi_e^{-}+\theta_I^{-}) \\ &\quad + Z_{\mathrm{c}}I_{\mathrm{t}}^{+}\sin(\delta^{+}+\delta^{-}+\phi_{\mathrm{c}}-\theta_I^{+}) \end{aligned} \tag{8}$$

where $\delta^{+} = \theta_{\mathrm{pll}}^{+} + \pi/6 - \theta_{\mathrm{g}}^{+}$ and $\delta^{-} = \theta_{\mathrm{pll}}^{-} + \pi/6 + \theta_{\mathrm{g}}^{+}$.

The dynamic equation of the PLL^{+} and PLL^{-} can be obtained from Fig. 1 as follows:

$$\delta^{+} = -\int (k_{\mathrm{p}}V_{tq}^{+} + k_i\int V_{tq}^{+}dt + \omega_0 - \omega_{\mathrm{g}})dt \tag{9}$$

$$\delta^{-} = -\int (k_{\mathrm{p}}V_{tq}^{-} + k_i\int V_{tq}^{-}dt - \omega_0 + \omega_{\mathrm{g}})dt. \tag{10}$$

Then, combining (7)–(10) and $\omega_0 = \omega_{\mathrm{g}}$, we can derive the dynamic block diagram of the system during asymmetric faults, as shown in Fig. 5.

It is suggested by Fig. 5 that the input of PLL^{+} and PLL^{-} (V_{tq}^{+} and V_{tq}^{-}) can be divided into two components: the PS/NS self-effect part and the PN sequence coupling effect part. The latter reflects the interaction between PS and NS synchronization dynamics. As shown in Fig. 5, when only PS currents are injected ($I_{\mathrm{t}}^{-} = 0$), there is no influence of the PN sequence coupling effect part on the PS PLL dynamics. However, it still influences the NS PLL dynamics and vice versa. Consequently, from the system perspective, the PN sequence coupling will affect the PSTS of the system, provided that the injection current is not zero.

By substituting (7) and (8) into (9) and (10), respectively, the fourth-order model of the system during asymmetric faults (represented as $\dot{\boldsymbol{x}} = f(\boldsymbol{x})$) can be expressed as

$$\begin{cases} d\delta^{+}/dt = -k_{\mathrm{p}}\{K_1V_{\mathrm{g}}^{+}\sin(\delta^{+}-\phi_1) + Z_{\mathrm{e}}^{+}I_{\mathrm{t}}^{+}\sin(\theta_I^{+}-\phi_{\mathrm{e}}^{+}) \\ \qquad +Z_{\mathrm{c}}I_{\mathrm{t}}^{-}\sin(\delta^{+}+\delta^{-}-\phi_{\mathrm{c}}-\theta_I^{-})\} - k_i x_{\mathrm{pll}}^{+} \\ dx_{\mathrm{pll}}^{+}/dt = K_1V_{\mathrm{g}}^{+}\sin(\delta^{+}-\phi_1) + Z_{\mathrm{e}}^{+}I_{\mathrm{t}}^{+}\sin(\theta_I^{+}-\phi_{\mathrm{e}}^{+}) \\ \qquad + Z_{\mathrm{c}}I_{\mathrm{t}}^{-}\sin(\delta^{+}+\delta^{-}-\phi_{\mathrm{c}}-\theta_I^{-}) \\ d\delta^{-}/dt = -k_{\mathrm{p}}\{K_2V_{\mathrm{g}}^{+}\sin(\delta^{-}+\phi_2) + Z_{\mathrm{e}}^{-}I_{\mathrm{t}}^{-}\sin(\phi_e^{-}+\theta_I^{-}) \\ \qquad +Z_{\mathrm{c}}I_{\mathrm{t}}^{+}\sin(\delta^{+}+\delta^{-}+\phi_c-\theta_I^{+})\} - k_i x_{\mathrm{pll}}^{-} \\ dx_{\mathrm{pll}}^{-}/dt = K_2V_{\mathrm{g}}^{+}\sin(\delta^{-}+\phi_2) + Z_{\mathrm{e}}^{-}I_{\mathrm{t}}^{-}\sin(\phi_e^{-}+\theta_I^{-}) \\ \qquad + Z_{\mathrm{c}}I_{\mathrm{t}}^{+}\sin(\delta^{+}+\delta^{-}+\phi_c-\theta_I^{+}) \end{cases} \tag{11}$$

where $\boldsymbol{x} = (\delta^{+}, x_{\mathrm{pll}}^{+}, \delta^{-}, x_{\mathrm{pll}}^{-})$, $x_{\mathrm{pll}}^{+} = \int V_{tq}^{+}dt$, and $x_{\mathrm{pll}}^{-} = \int V_{tq}^{-}dt$.

The presence of an available EP during asymmetric fault is a prerequisite for the stable operation of the system. The issue of available EP existence has been investigated in [24] and [25]. This article mainly concentrates on transient process analysis, which determines whether the operation point of the system can eventually reach the available EP during asymmetric fault from the prefault state. Thus, in this article, it is assumed that there exists an available EP $\mathbf{x_e}$ for the system during asymmetric faults, where $\mathbf{x_e} = (\delta_{\mathrm{e}}^{+},\ 0,\ \delta_{\mathrm{e}}^{-},\ 0)$.

C. Validation of the Fourth-Order Model and Transient Instability Phenomenon

To validate the fourth-order model (11) and demonstrate the necessity and motivation of this study, a switching model of the system depicted in Fig. 1 was developed in PSCAD/EMTDC. Table I summarizes four different conditions, and Table V in Appendix C lists the other parameters. The corresponding short-circuit ratio (SCR) for all four operating conditions is 1.1. For the four conditions, Fig. 6 shows the simulation results for the detailed switching model (**red solid line**), the fourth-order model (11) (**blue dotted line**), and the reduced-order model ignoring PN sequence coupling in [20] (**black dashed line**). From Fig. 6, the conclusions can be obtained as follows.

1) Fourth-Order Model (11) Can be Used to Analyze PSTS of the System Under Asymmetric Faults: From Fig. 6(a)–(d), the proposed model (11) closely approximates the detailed switching model for all four conditions, with highly coincident results when the system is stable. These results confirm the effectiveness of the simplified model (11) in analyzing the PSTS of the system under asymmetric faults.

2) PN Sequence Coupling Significantly Affects the PSTS of the WG-VSC System: For Case 1, an unstable case may be mistaken for stable by the model in [20], which ignores the PN sequence coupling, as demonstrated in Fig. 6(a). Similarly, for Case 3, the simulation in Fig. 6(c) shows that the WG-VSC system during DLG fault is stable. However, ignoring the influence of the PN sequence coupling can lead to an incorrect conclusion that the system will undergo NS-dominated PLL synchronization transient instability. Thus, to obtain a more accurate stability assessment, the effect of PN sequence coupling on the PSTS of the system must be considered during asymmetric faults.

TABLE I
SIMULATION CONDITIONS OF CASES 1–4

Case	Set asymmetric grid fault at t=0.5 s	Current references in fault-on state $\{I_{td\text{ref}}^{+}, I_{tq\text{ref}}^{+}, I_{td\text{ref}}^{-}, I_{tq\text{ref}}^{-}\}$		Stable or not?
		At t=0.5s	At t=4.5s	
Case 1	**SLG**	{0.75, 0.5, 0, 0.5} pu	remain unchanged	**Unstable**
Case 2		{0.75, 0.5, 0, 0} pu	{0.75, 0.5, 0, 0.5} pu	Stable
Case 3	**DLG**	{0.4, 0.5, −0.3, −0.5} pu	{0.4, 0.5, −0.38, −0.5} pu	Stable
Case 4		{0.4, 0.5, −0.38, −0.5} pu	remain unchanged	**Unstable**

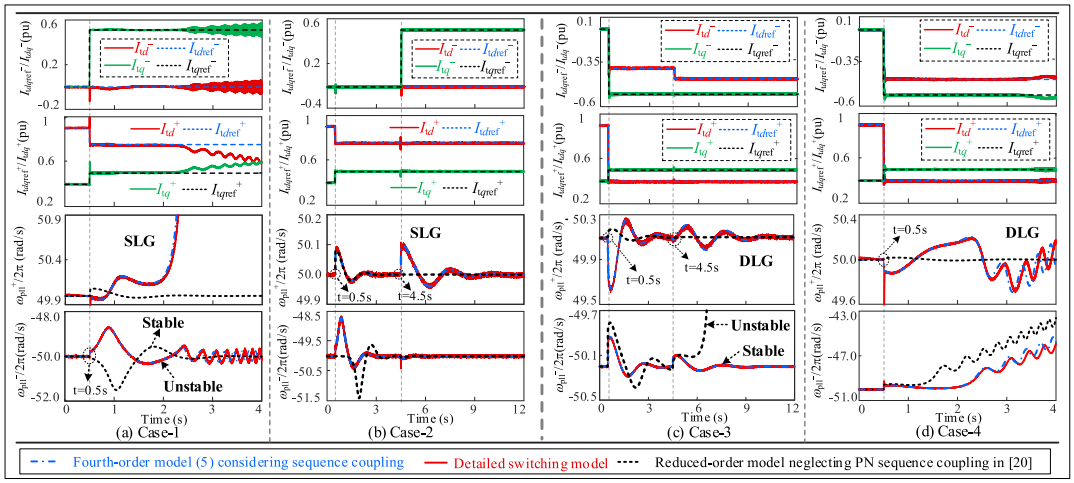

Fig. 6. Simulation results. (a) Case 1. (b) Case 2. (c) Case 3. (d) Case 4.

3) Available EP Exists During Asymmetric Faults, But PLL Synchronization Unstable Occurs: The simulation results of Cases 1 and 2 are shown in Fig. 6(a) and (b), respectively. In Case 1, when current references are directly adjusted to $I_{td\text{ref}}^{+} = 0.75$ pu, $I_{tq\text{ref}}^{+} = 0.5$ pu, and $I_{tq\text{ref}}^{-} = 0.5$ pu at $t =$ 0.5 s, synchronization of both PLL^{-} and PLL^{+} cannot remain, implying that PLL synchronization is unstable. In Case 2, when current references are changed to those same values in Case 2 at two different times, the system is stable. The simulation result of Case 2 suggests that for Case 1, an available EP exists, but PLL synchronization unstable still occurs.

Similarly, as shown in Fig. 6(d) (related to Case 4), loss of PSTS occurs when $I_{td\text{ref}}^{-}$ is directly changed to -0.38 pu at $t =$ 0.5 s. While the system is stable when $I_{td\text{ref}}^{-}$ is first selected as -0.3 pu at $t = 0.5$ s and further increased to -0.38 pu at $t =$ 4.5 s, as shown in Fig. 6(c) (related to Case 3). Thus, Fig. 6(c) and (d) suggests that PLL synchronization unstable can still appear during asymmetric faults, even if an available EP exists.

Given the above analysis, it is necessary to investigate the PSTS of the WG-VSC system considering PN sequence coupling. However, in the published works, few researchers have analyzed this issue, which is an essential research motivation for this article.

III. PSTS ANALYSIS OF WG-VSC SYSTEM BASED ON LEDA

In this section, we provide a theoretical explanation of the PSTS and instability phenomena in Fig. 6 based on the LEDA of the system during asymmetric faults. To the best knowledge of authors, theoretical exploration of this phenomenon has been lacking in previous research. Note that the LEDA can be constructed with the linear matrix inequality (LMI) optimization method [27], the sum-of-squares (SOS) programming method [28], or the TS method [31]. The comparison of runtimes and volumes of the LEDA constructed based on LMI, SOS, and TS methods has been provided in Appendix E. Considering the computational burden and conservativeness, the TS method is used to construct the LEDA in this article.

A. Constructing LEDA With the TS Method

The fourth-order model (11) shows that only two state variables, x_l (l = 1,3), contribute to the nonlinear behavior of the system, specifically $x_1 = \delta^{+}$ and $x_3 = \delta^{-}$. Thus, in this article, the TS fuzzy model of the nonlinear fourth-order model (11) is first constructed in the region $\psi = \{\boldsymbol{x} \in \mathbb{R}^4 | \, x_{l\min} \le x_l \le x_{l\max}\}$, as expressed in the following equation (for detailed information on the construction process, please refer to Appendix D):

$$\dot{\boldsymbol{x}} = \sum_{i=1}^{2^4} h_i(x_1, x_3) \boldsymbol{A}_i (\boldsymbol{x} - \mathbf{x_e}) \tag{12}$$

where the expressions of $\boldsymbol{A}_i$ and h_i (x_1, x_3) can be seen in (D4) and (D6) of AppendixD, respectively.

For all matrices $\boldsymbol{A}_i$ in (12), if there exists a symmetric positive definite matrix $\boldsymbol{M}$, $\boldsymbol{M} \in \mathbb{R}^{4\times4}$, satisfying LMIs (13). Then, $\Omega = \{\boldsymbol{x} \in \mathbb{R}^4 | \; v(\boldsymbol{x}) \le \min \; v(\partial\psi)\}$ is a subset of the real domain of attraction (DA) of the system (11). This subset is considered as an estimated DA, where $v(\boldsymbol{x}) = (\boldsymbol{x} - \mathbf{x_e})^{\mathrm{T}} \boldsymbol{M} (\boldsymbol{x} - \mathbf{x_e})$ is a Lyapunov

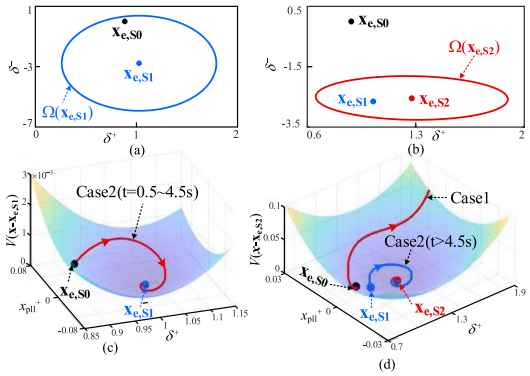

Fig. 7. Projected on the $\delta^+ - \delta^-$ plane. (a) $\Omega_V(\mathrm{x_{e,S1}})$. (b) $\Omega_V(\mathrm{x_{e,S2}})$; trajectory in $\delta^+ - x_{\mathrm{pll}}^+$ plane. (c) Case 2 ($t = 0.5$–4.5 s). (d) Case 2 ($t = 0.5$–4.5 s) and Case 1.

Algorithm 1: LEDA Construction With TS Method.

Input: fourth-order model (11), step size Δx_l.

Initialization: Let $x_{1\min} = x_{1\max} = \delta_{\mathrm{e}}^+$, $x_{3\min} = x_{3\max} = \delta_{\mathrm{e}}^-$.

(1) Constructing the TS fuzzy model of (11) in region ψ.

while LMIs (13) is feasible **do**

(2) Solve LMIs (13) for $\boldsymbol{M}$.

(3) Enlarge region ψ: $x_{l\min} = x_{l\min} - \Delta x_l$, $x_{l\max} = x_{l\max} + \Delta x_l$.

(4) Reconstructing the TS fuzzy model of (11) in region ψ.

End

(5) Optimum Lyapunov function $V(\boldsymbol{x}) = (\boldsymbol{x} - \mathbf{x_e})^{\mathrm{T}} \boldsymbol{M} (\boldsymbol{x} - \mathbf{x_e})$.

(6) Calculate critical level set $V_{\mathrm{cr}} = \min V(\partial\psi)$

Output: The LEDA of (11): $\Omega_V = \{ \boldsymbol{x} \in \mathbb{R}^4 | \ V(\boldsymbol{x}) \le V_{\mathrm{cr}} \}$.

function of the system (11), $\partial\psi$ is the boundary of ψ

$$\begin{cases} \boldsymbol{M} = \boldsymbol{M}^{\mathrm{T}} > 0 \\ \boldsymbol{A}_i^{\mathrm{T}} \boldsymbol{M} + \boldsymbol{M} \boldsymbol{A}_i < 0, \forall i \in \{1, 2, \ldots, 2^4\} \end{cases}. \tag{13}$$

The estimated DA Ω can be expanded by iteratively decreasing $x_{l\min}$ and increasing $x_{l\max}$ while solving the LMIs (13). The largest Ω, LEDA, is obtained when the LMIs (13) are no longer feasible.

Based on the above analysis, an algorithm for constructing the LEDA of the system with the TS method can be obtained, referred to as Algorithm 1.

Once the LEDA at the available EP $\mathbf{x_{e,1}}$ of the fault-on state is obtained by Algorithm 1, the stability of the transient process in which the operation point transits from the original EP of prefault state $\mathbf{x_{e,0}}$ to $\mathbf{x_{e,1}}$ can be judged by the following criterion:

$$V(\mathbf{x_{e,0}}) \le V_{\mathrm{cr}}. \tag{14}$$

Suppose criterion (14) is satisfied. In that case, it indicates that $\mathbf{x_{e,0}}$ is located within or on the boundary of the LEDA at $\mathbf{x_{e,1}}$, which implies that the transient process of the system from $\mathbf{x_{e,0}}$ to $\mathbf{x_{e,1}}$ must be transient stability. Otherwise, there is a risk of PLL synchronization transient instability.

B. Theoretical Explanation of the Transient Stability and Instability Phenomenon in Fig. 6 Based on the LEDA

In this section, the theoretical explanation of the PSTS and instability phenomena in Fig. 6 is presented based on the LEDA obtained by Algorithm 1. Also, we define the available EPs associated with $t<0.5$ s, $t = 0.5$–4.5 s, $t>4.5$ s of Cases 2 and 3 as $\mathbf{x_e}_{,\mathrm{S0}}$, $\mathbf{x_e}_{,\mathrm{S1}}$, and $\mathbf{x_e}_{,\mathrm{S2}}$ and $\mathbf{x_e}_{,\mathrm{D0}}$, $\mathbf{x_e}_{,\mathrm{D1}}$, and $\mathbf{x_e}_{,\mathrm{D2}}$, respectively.

For Cases 1 and 2, the LEDA of the EPs $\mathbf{x_e}_{,\mathrm{S1}}$ and $\mathbf{x_e}_{,\mathrm{S2}}$ are obtained by Algorithm 1, denoted as $\Omega_V(\mathbf{x_e}_{,\mathrm{S1}})$ and $\Omega_V(\mathbf{x_e}_{,\mathrm{S2}})$, respectively. Their projections on the $\delta^+ - \delta^-$ plane are depicted in Fig. 7(a) and (b), respectively. According to Fig. 7, it can be seen that $\boldsymbol{X}_{\mathbf{e},\mathrm{S0}}$ lies within $\Omega_V(\mathbf{x_e}_{,\mathrm{S1}})$ and $\mathbf{x_e}_{,\mathrm{S1}}$ lies within $\Omega_V(\mathbf{x_e}_{,\mathrm{S2}})$. Thus, for the transient process of Case 2 in which the operation point is transitioned from $\mathbf{x_e}_{,\mathrm{S0}}$ to $\mathbf{x_e}_{,\mathrm{S1}}$ and then to $\mathbf{x_e}_{,\mathrm{S2}}$, the Lyapunov functions value of the system must decrease gradually with the system trajectory and eventually converge to zero, as illustrated in Fig. 7(c) and (d). The transient process of Case 2 must be PSTS.

Fig. 7(b) shows that $\mathbf{x_e}_{,\mathrm{S0}}$ is located outside of $\Omega_V(\mathbf{x_e}_{,\mathrm{S2}})$. Thus, for the transient process of Case 1 in which the operation point is transitioned directly from $\mathbf{x_e}_{,\mathrm{S0}}$ to $\mathbf{x_e}_{,\mathrm{S1}}$, the Lyapunov function value of the system may increase gradually with the system trajectory. The system trajectory will gradually move away from $\mathbf{x_e}_{,\mathrm{S2}}$, and the transient process of Case 1 will be unstable, as shown in Fig. 7(d). The above results theoretically explain the PLL synchronization transient instability and stable phenomenon in Fig. 6(a) and (b).

From the theoretical analyses of Fig. 7(a) and (b), it is clear that the reason that the first transient process of Case 2 ($t = 0.5$–4.5 s) is transient stable but Case 1 is transiently unstable is that $\Omega_V(\mathbf{x_e}_{,\mathrm{S1}})$ is larger than $\Omega_V(\mathbf{x_e}_{,\mathrm{S2}})$, leading to the fact that $\mathbf{x_e}_{,\mathrm{S0}}$ is located inside of $\Omega_V(\mathbf{x_e}_{,\mathrm{S1}})$ but outside of $\Omega_V(\mathbf{x_e}_{,\mathrm{S1}})$. The explanation of why $\Omega_V(\mathbf{x_e}_{,\mathrm{S1}})$ is larger than $\Omega_V(\mathbf{x_e}_{,\mathrm{S2}})$ from the physical mechanism aspect is provided in Appendix F.

For Cases 3 and 4, the LEDA at the EPs $\mathbf{x_e}_{,\mathrm{D1}}$ and $\mathbf{x_e}_{,\mathrm{D2}}$, denoted as $\Omega_V(\mathbf{x_e}_{,\mathrm{D1}})$ and $\Omega_V(\mathbf{x_e}_{,\mathrm{D2}})$ are projected on the $\delta^+ - \delta^-$ plane as shown in Fig. 8(a) and (b), respectively.

As indicated in Fig. 8, $\mathbf{x_e}_{,\mathrm{D0}}$ and $\mathbf{x_e}_{,\mathrm{D1}}$ are located in $\Omega_V(\mathbf{x_e}_{,\mathrm{D1}})$ and $\Omega_V(\mathbf{x_e}_{,\mathrm{D2}})$, respectively. Thus, it can be determined that the operation point of the system can transition from $\mathbf{x_e}_{,\mathrm{D0}}$ to $\mathbf{x_e}_{,\mathrm{D1}}$ and further to $\mathbf{x_e}_{,\mathrm{D2}}$ while maintaining transient stability. The transient process for Case 3 must be transient stability, as shown in Fig. 8(c) and (d). However, as shown in Fig. 8(b), $\mathbf{x_e}_{,\mathrm{D0}}$ is located outside of $\Omega_V(\mathbf{x_e}_{,\mathrm{D2}})$, indicating a potential instability of the transient process for Case 4. The evolution of the Lyapunov functions value with the system trajectory for Case 4 is provided in Fig. 8(d). As observed, the Lyapunov function value gradually diverges with the system trajectory, and thus Case 4 is PLL synchronization transient instability. The simulation results shown in Fig. 6(c) and (d) are consistent with the above theoretical analysis.

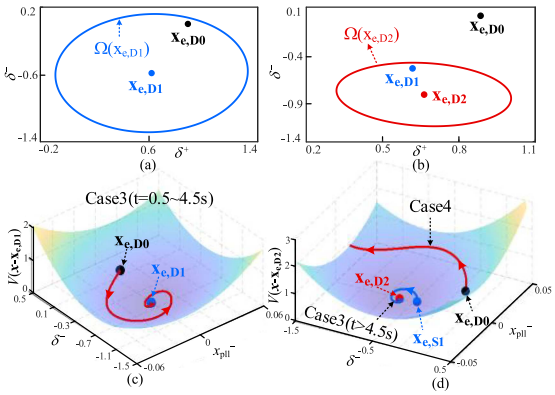

Fig. 8. Projected on the $\delta^+-\delta^-$ plane. (a) $\Omega_V(X_{e,D1})$. (b) $\Omega_V(X_{e,D2})$; trajectory in $\delta^- - x_{pll}^-$ plane. (c) Case 3 ($t = 0.5$–4.5 s). (d) Case 3 ($t = 0.5$–4.5 s) and Case 4.

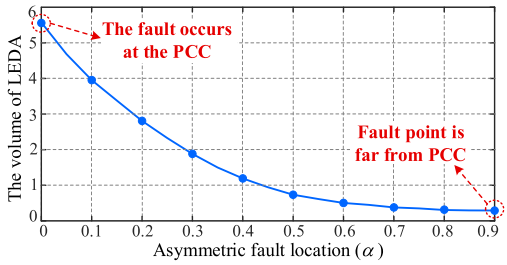

Fig. 9. Varying trend of the volume of LEDA with α.

C. Analysis of the Influence of Fault Location on PSTS

With the LEDA of the system, it becomes possible to quantitatively analyze the effect of specific parameters on the PSTS of the system. This analysis involves comparing the volume of the LEDA under different system parameters. A larger volume of the LEDA implies improved PSTS. In this section, the impact of fault location on the transient stability of the system is analyzed.

The LEDA constructed by the TS method is a hyper ellipsoid with the volume calculated as follows:

$$\mathrm{Vol} = \pi^2/\Gamma(3)\sqrt{\mathrm{V_{cr}}\prod_{i=1}^{4}(\lambda_i)^{-1}} \tag{15}$$

where λ_i is the eigenvalues of the matrix $\boldsymbol{M}$ and Γ is the gamma function.

In this article, the coefficient α as shown in (16) is defined to reflect the fault location. Obviously, the smaller α is, the closer the fault point is to the PCC. $\alpha = 0$ implies that asymmetrical fault occurs at PCC as

$$\alpha = \boldsymbol{Z_L}/(\boldsymbol{Z_L}+\boldsymbol{Z_g}). \tag{16}$$

Considering an LL fault, the current references are selected to $I_{td\mathrm{ref}}^{+} = 0.6$ pu, $I_{tq\mathrm{ref}}^{+} = 0.5$ pu, $I_{td\mathrm{ref}}^{-} = 0$ pu, and $I_{tq\mathrm{ref}}^{-} = 0.4$ pu. Maintaining the SCR as constant, α increasing from 0 to 0.9 (fault location gradually moving away from PCC), the varying trend of the volume of LEDA can be obtained as shown in Fig. 9.

As shown in Fig. 9, when the fault location is away from the PCC, the volume of LEDA is reduced, indicating a deterioration in the transient synchronization stability.

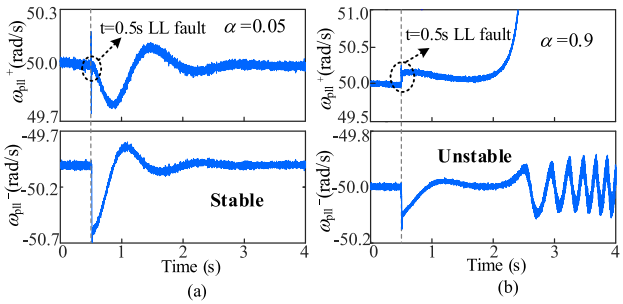

Fig. 10. Simulation results under scenarios: (a) $\alpha = 0$ and (b) $\alpha = 0.9$.

To validate the above analyses, the PSCAD/EMTDC simulation results under two different scenarios, $\alpha = 0$ and $\alpha = 0.9$, are provided in Fig. 10(a) and (b), respectively. From Fig. 10(a), the system can maintain transient stability when the fault occurs at the PCC ($\alpha = 0$). However, if the fault location is far away from the PCC ($\alpha = 0.9$), VSC is unable to maintain synchronization with the grid and the system is transiently unstable, as illustrated in Fig. 10(b). This agrees with the theoretical analysis results based on Fig. 9, confirming the validity of the above analysis.

The PSTS of the system can be evaluated using the LEDA at the available EP of the system. However, the LEDA is constructed in the state space and can only analyze the PSTS of the WG-VSC system for a specific current injection strategy, as shown in Figs. 7 and 8. Thus, the LEDA does not provide practical guidelines for designing and adjusting current injection reference during fault ride-through. Consequently, there is an urgent need to construct the FR-PNC in the space of PN sequence injection currents from the PSTS point of the system during asymmetric faults. The details of the FR-PNC will be presented in the next section.

IV. Construction and Influence Analysis of the Feasible Region of Positive and Negative Currents

Considering PN sequence coupling, the FR-PNC of the system is constructed in this section with the obtained LEDA in Section III. Due to the inherent 4-D nature of the FR-PNC, which is defined in the parameter space of PN sequence active and reactive currents, direct visualization poses significant challenges. To address this, an algorithm is proposed to visualize this FR-PNC in a 2-D subspace. The influence of PN sequence coupling on the FR-PNC is then analyzed, considering different fault positions. Moreover, the influence of PN sequence injection currents on the PSTS of the system is visually analyzed based on FR-PNC. Finally, experiment results obtained from the RT-Box hardware-in-the-loop (HIL) platform, as depicted in Fig. 11, are presented to validate the theoretical analysis.

A. Construction of the FR-PNC for the WG-VSC System

The definition of FR-PNC was provided in [20] for the first time, which can be described as follows.

The FR-PNC is a 4-D region in PS and NS injection currents space that satisfies the PSTS constraint (I), maximum current

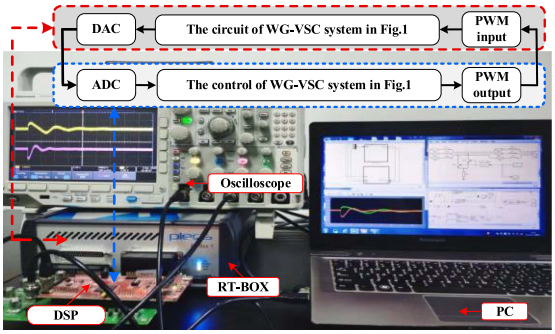

Fig. 11. RT-Box HIL platform.

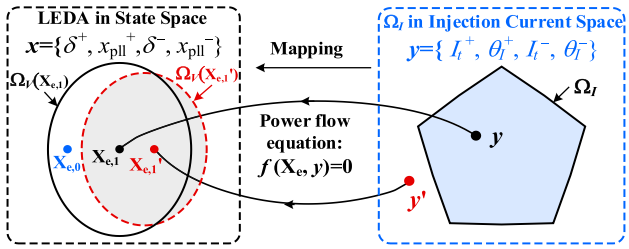

Fig. 12. Distinction and correlation between the FR-PNC and the LEDA.

constraint (II), and PCC voltage constraint (III) simultaneously. The FR-PNC, denoted as Ω_I, can be mathematically written as

$$\Omega_I \triangleq \Psi_{\mathrm{I}} \cap \Psi_{\mathrm{II}} \cap \Psi_{\mathrm{III}} \tag{17}$$

where Ψ_{I}, Ψ_{II}, and Ψ_{III} represent the feasible region of PS and NS injection currents that satisfy the PSTS constraint (I), maximum current constraint (II), and PCC Voltage constraint (III), respectively.

Ψ_{I}, Ψ_{II}, and Ψ_{III} can be expressed as

$$\Psi_{\mathrm{I}} = \left\{ (\boldsymbol{I}_{\mathrm{t}}^{+}, \boldsymbol{I}_{\mathrm{t}}^{-}) \middle| V(\mathbf{x_{e,0}} - \mathbf{x_{e,1}}) \le V_{\mathrm{cr}} \right\} \tag{18}$$

$$\Psi_{\mathrm{II}} = \left\{ (\boldsymbol{I}_{\mathrm{t}}^{+}, \boldsymbol{I}_{\mathrm{t}}^{-}) \middle| \mathrm{I_{tmax}} \le \mathrm{I}_m, \mathrm{I_{tmax}} = \max\{\mathrm{I_{tx}}\} \right\} \tag{19}$$

$$\Psi_{\mathrm{III}} = \left\{ (\boldsymbol{I}_{\mathrm{t}}^{+}, \boldsymbol{I}_{\mathrm{t}}^{-}) \middle| V_{tde,1}^{+} > 0,\ V_{tde,1}^{-} > 0 \right\} \tag{20}$$

where subscript x in (19) denotes phases a, b, and c, $\boldsymbol{I}_{\mathrm{t}x}$ denotes the steady-state injected current of phase x for VSC under asymmetric fault, an $V_{tde,1}^{+}$ and $V_{tqe,1}^{-}$ denote d-axis components of PS and NS PCC voltage, respectively.

The expression of $\boldsymbol{I}_{\mathrm{t}x}$ (x = a, b, c) is given in the following equation, and a detailed derivation can be seen in [20]:

$$\boldsymbol{I}_{\mathrm{tx}} = \sqrt{(I_{\mathrm{t}}^{+})^2 + (I_{\mathrm{t}}^{-})^2 + 2I_{\mathrm{t}}^{+}I_{\mathrm{t}}^{-}\cos(\theta_I^{+} + \theta_I^{-} - \delta_{\mathrm{e}}^{+} - \delta_{\mathrm{e}}^{-} + \lambda_{\mathrm{x}})} \tag{21}$$

where λ_{a}, λ_{b}, and λ_{c} correspond to 0, 240°, and 120°, respectively.

According to (5) and (6), $V_{tde,1}^{+}$ and $V_{tde,1}^{-}$ can be expressed as

$$\begin{aligned} V_{tde,1}^{+} = {} & K_1 V_{\mathrm{g}}^{+}\cos(\delta_{\mathrm{e},1}^{+} - \phi_1) + Z_{\mathrm{e}}^{+} I_{\mathrm{t}}^{+}\cos(\theta_I^{+} - \phi_{\mathrm{e}}^{+}) \\ & + Z_{\mathrm{c}} I_{\mathrm{t}}^{-}\cos(\delta_{\mathrm{e},1}^{+} + \delta_{\mathrm{e},1}^{-} - \phi_{\mathrm{c}} - \theta_I^{-}) \end{aligned} \tag{22}$$

$$\begin{aligned} V_{tde,1}^{-} = {} & K_2 V_{\mathrm{g}}^{+}\cos(\delta_{\mathrm{e},1}^{-} + \phi_2) + Z_{\mathrm{e}}^{-} I_{\mathrm{t}}^{-}\cos(\phi_e^{-} + \theta_I^{-}) \\ & + Z_{\mathrm{c}} I_t^{+}\cos(\phi_{\mathrm{c}} - \theta_I^{+} + \delta_{\mathrm{e},1}^{+} + \delta_{\mathrm{e},1}^{-}). \end{aligned} \tag{23}$$

Combined with (18)–(23), the FR-PNC considering PN sequence coupling can be numerically constructed.

Fig. 12 shows the distinction and correlation between the FR-PNC (Ω_I) and the LEDA. The specific expression for $f(\mathbf{x_e}, \boldsymbol{y})$ in Fig. 12 is given in (11).

In Fig. 12, we define $\boldsymbol{y} = (y_1, y_2, y_3, y_4) = (I_{\mathrm{t}}^{+}, \theta_I^{+}, I_{\mathrm{t}}^{-}, \theta_I^{-})$. The detailed explanation of Fig. 12 is as follows.

1) Each point $\boldsymbol{y}$ in the PN sequence injection currents space has a unique corresponding available EP $\mathbf{x_{e,1}}$ in the state space if it exists. The mapping relationship between $\boldsymbol{y}$ and $\mathbf{x_{e,1}}$ is given by $f(\mathbf{x_{e,1}}, \boldsymbol{y}) = 0$.
2) If any point $\boldsymbol{y}$ in the space of PN sequence injection currents is in the FR-PNC (ΩI), then the prefault state $\mathbf{x_{e,0}}$ is located within the LEDA ($\Omega_V(\mathbf{x_{e,1}})$) at the available EP $\mathbf{x_{e,1}}$, which is determined by $\boldsymbol{y}$. That is, if PN sequence injection currents fall within ΩI, the system must be PSTS during asymmetric faults.

The dimension of the FR-PNC is 4, which is difficult to visualize directly. Thus, we propose a simple approach to visualize the range and constraints of the FR-PNC by giving any two variables of $\boldsymbol{y}$ and projecting the FR-PNC onto the space of the remaining two variables. Note that the projection can be adjusted according to specific needs.

Next, an algorithm to visualize the FR-PNC in a 2-D subspace is provided in this article.

B. Visualization of FR-PNC in 2-D Subspaces

In this article, the double-layer circulation method is proposed to visualize FR-PNC in the 2-D subspace y_i-y_j ($i, j = 1, \ldots, 4$, $i \neq j$) with given y_m, y_n ($m, n = 1, \ldots, 4$, $m \neq n$, $m \neq i,j$, $n \neq i,j$), as shown in Fig. 13.

In Fig. 13, $y_{i\max}$ and $y_{j\max}$ denote the maximum values of y_i and y_j, respectively. The maximum values of current phase angles y_2 and y_4 are 360°. y_1 and y_3 represent the current amplitude, and the maximum values are given as I_{m} in this article. Moreover, Δy_i and Δy_j are the step sizes of y_i and y_j, respectively. In consideration of balancing time consumption and calculation accuracy, Δy_1, Δy_2, Δy_3, and Δy_4 are set to 0.05pu, 1°, 0.02 pu, and 1°, respectively.

Next, the influence of PN sequence coupling on FR-PNC with different fault positions will be discussed in Section IV-C. Note that the projection of the FR-PNC in PS/NS current space is a representation of the PSTS of the system during asymmetric faults. Thus, the impact of PS and NS injection currents on the PSTS of the system will be analyzed visually in Sections IV-D and Section IV-E based on FR-PNC. Since fault type will not affect subsequent analysis, the DLG fault is taken as an example.

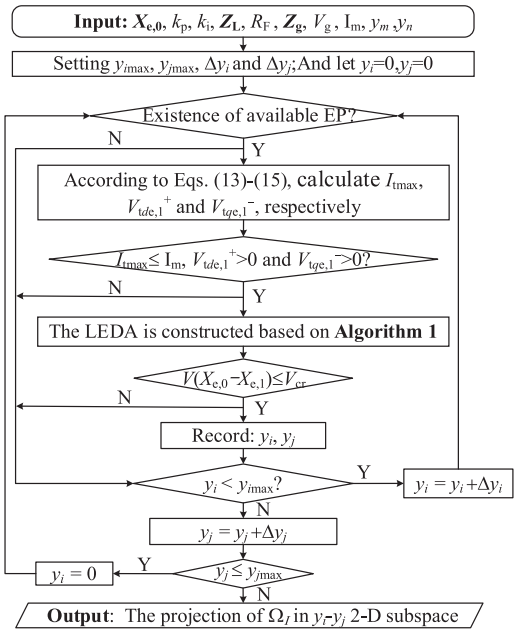

Fig. 13. Double-layer circulation method for visualizing the FR-PNC.

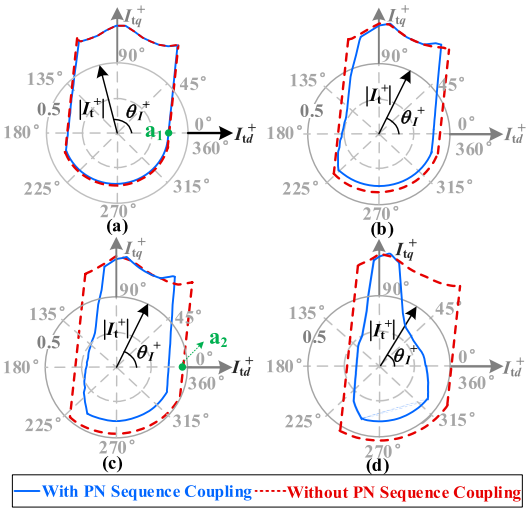

Fig. 14. Visualized boundaries of FR-PNC in the positive sequence current space. (a) $\alpha = 0.95$. (b) $\alpha = 0.67$. (c) $\alpha = 0.33$. (d) $\alpha = 0.1$.

C. Analysis of the Influence of PN Sequence Coupling on FR-PNC With Different Fault Locations

To visually show the effect of PN sequence coupling on FR-PNC with different fault locations, this article considers four scenarios with α selected to be 0.95, 0.67, 0.33, and 0.1. Note that for all four scenarios, the SCR remains constant at 1.1 (the sum of Z_L and Z_g remains unchanged). With $\boldsymbol{I}_t^-$ is given as $0.3j$ pu, Fig. 14(a)–(d) compares the visualized boundaries of FR-PNC considering PN sequence coupling in this article with the FR-PNC ignoring it in [20] on PS current space for the above four scenarios, respectively.

Fig. 14(a) shows that when the fault location is far from the PCC ($\alpha = 0.95$), the impact of PN sequence coupling on the FR-PNC in the positive sequence current space is negligible. This observation confirms the justification for neglecting PN sequence coupling in prior work [20]. However, as the fault point moves closer to the PCC, Fig. 14(b)–(d) reveals that the effect of PN sequence coupling on the FR-PNC boundary becomes more significant. The result in Fig. 14(b)–(d) implies that the effect of PN sequence coupling must be considered for a more general case. Thus, the results of this study provide an essential reference for understanding the effect of PN sequence coupling on the PSTS of the system during asymmetric faults.

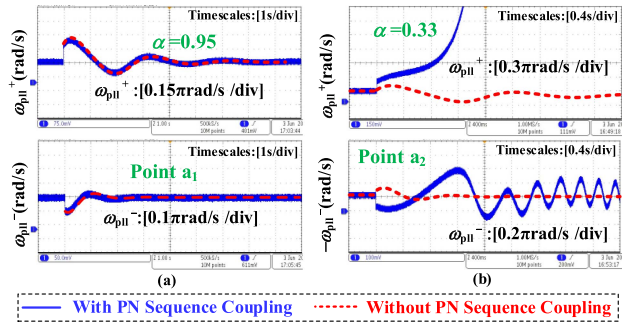

Fig. 15. Experimental results under scenarios (a) Point $\mathbf{a}_1$ ($\boldsymbol{I}_\mathbf{t}^+ = 0.35 \angle 0°$). (b) Point $\mathbf{a}_2$ ($\boldsymbol{I}_\mathbf{t}^+ = 0.45 \angle 0°$).

To validate the theoretical analysis results, this study presents RT-Box HIL experimental results for two different scenarios. Specifically, specific operating parameters ($I_t^+, \theta_I^+, \alpha$) selected to be (0.35, 0°, 0.95) and (0.45, 0°, 0.33), corresponding to the points a_1 and a_2 in Fig. 14(a) and (c), respectively. The experimental results are presented in Fig. 15. Furthermore, the results the of reduced-order model in our prior work [20], which neglects PN sequence coupling, are also provided in Fig. 15 for comparison.

The results presented in Fig. 15 reveal important insights into the effect of PN sequence coupling on the PSTS of the system under asymmetric faults. For operating point a_1, it is observed that experimental results and the model ignoring PN sequence coupling are highly coincident. This result suggests that the effect of PN coupling on the PSTS of the system is negligible in the scenario of fault points far from the PCC point. However, for operating point a_2, where the fault location is close to the PCC. The experimental results in Fig. 15(b) demonstrate that neglecting PN sequence coupling can result in the misjudgment of an unstable case as transient stability. Thus, PN sequence coupling must be considered in such scenarios to accurately assess system stability. The agreement between the results in Fig. 15 and the theoretical analysis in Fig. 14 provides strong evidence for the validity of the proposed theoretical analysis in this article.

D. Visualization of FR-PNC in Positive-Sequence Current Space With Different Negative-Sequence Injection Currents

To visually demonstrate the impact of different NS currents on the PSTS of the system, Fig. 16(a)–(d) presents the visualization

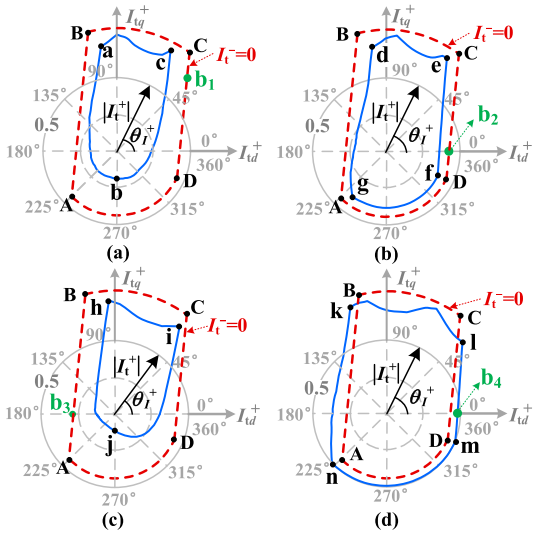

Fig. 16. Visualization of FR-PNC in PS injection current space. (a) $\boldsymbol{I}_{\mathbf{t}}^{-} = 0.3 \angle 0°$ ($\boldsymbol{I}_{\mathbf{td}}^{-} = 0.3$ pu). (b) $\boldsymbol{I}_{\mathbf{t}}^{-} = 0.3 \angle 90°$ ($\boldsymbol{I}_{\mathbf{tq}}^{-} = 0.3$ pu). (c) $\boldsymbol{I}_{\mathbf{t}}^{-} = 0.3 \angle 180°$ ($\boldsymbol{I}_{\mathbf{td}}^{-} = -0.3$ pu). (d) $\boldsymbol{I}_{\mathbf{t}}^{-} = 0.3 \angle 270°$ ($\boldsymbol{I}_{\mathbf{tq}}^{-} = -0.3$ pu).

TABLE II
EFFECT OF DIFFERENT NS INJECTION CURRENTS ON PSTS

$\boldsymbol{I}_{\mathbf{t}}^{-}$	Characterization of NS injection current	Impact of PSTS
$0.3\angle 0°$	Injecting of NS active current	Deterioration
$0.3\angle 90°$	Injecting of NS reactive current	Deterioration
$0.3\angle 180°$	Absorbing of NS active current	Deterioration
$0.3\angle 270°$	**Absorbing of NS reactive current**	**Improvement**

boundaries of FR-PNC in PS current space with $\alpha = 0.5$ and $\boldsymbol{I}_{\mathbf{t}}^{-}$ selected to be $0.3 \angle 0°$, $0.3 \angle 90°$, $0.3 \angle 180°$, and $0.3 \angle 270°$, corresponding to regions R_{abc}, R_{defg}, R_{hij}, and R_{knml}, respectively. For comparison, Fig. 16 also provides the visualized boundary of the FR-PNC in PS current space with $\boldsymbol{I}_{\mathbf{t}}^{-} = \mathbf{0}$, corresponding to region R_{ABCD} (red dashed line).

From Fig. 16, it can be seen that: 1) when NS reactive current is absorbed by the VSC, the FR-PNC is enlarged, indicating an improvement in PSTS of the system; and 2) when NS reactive current is injected, or NS active current is injected/absorbed by the VSC, the FR-PNC is reduced, indicating a deterioration in transient stability of the system. These valuable insights hold significant potential for informing the design of control strategies aimed at enhancing the transient stability of the system under asymmetric faults. The above results are summarized in Table II.

These findings about the influence of NS current on the PSTS of the system have been verified by experimental results. Specifically, points b_1, b_2, and b_3 shown in Fig. 16(a)–(c), corresponding to three different scenarios with specific operating parameters (I_{t}^{+}, θ_I^{+}) selected to be (0.69, 47°), (0.42, 0°), and (0.275, 180°), respectively. These points are all on the boundary of regions R_{ABCD} but located outside the regions R_{abc}, R_{defg}, and R_{hij}, respectively. Thus, the system is transient stability under the scenarios when $\boldsymbol{I}_{\mathbf{t}}^{-} = \mathbf{0}$. However, if $\boldsymbol{I}_{\mathbf{t}}^{-}$ is selected to be $0.3 \angle 0°$, $0.3 \angle 90°$, and $0.3 \angle 180°$, respectively,

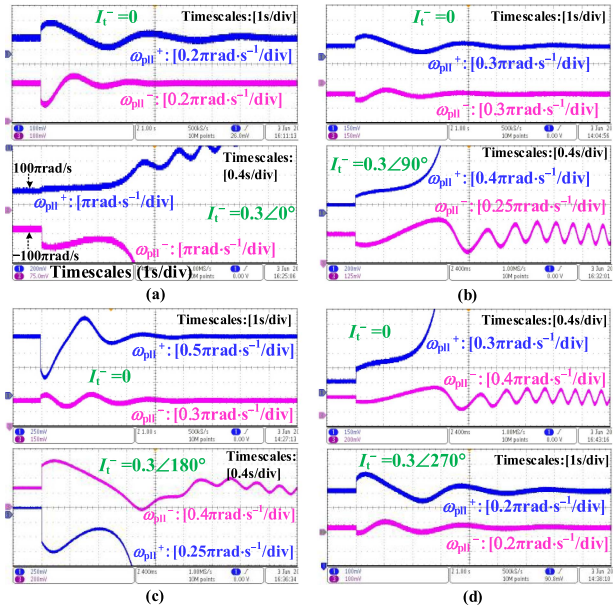

Fig. 17. Experimental results: (a) Point $\mathbf{b}_1(\boldsymbol{I}_{\mathbf{t}}^{+} = 0.69 \angle 47°)$. (b) Point $\mathbf{b}_2(\boldsymbol{I}_{\mathbf{t}}^{+} = 0.42 \angle 0°)$. (c) Point $\mathbf{b}_3(\boldsymbol{I}_{\mathbf{t}}^{+} = 0.275 \angle 180°)$. (d) Point $\mathbf{b}_4(\boldsymbol{I}_{\mathbf{t}}^{+} = 0.48 \angle 0°)$.

PLL synchronization transient instability will occur in these scenarios. The experimental results presented in Fig. 17(a)–(c) confirm the theoretical analysis results above.

For point b_4, as illustrated in Fig. 16(d), the values of I_{t}^{+} and θ_I^{+} set to 0.48 and 0, respectively. Fig. 17(d) demonstrates that the system is transient stability with $\boldsymbol{I}_{\mathbf{t}}^{-} = 0.3 \angle 270°$ at point b_4. However, adjusting $\boldsymbol{I}_{\mathbf{t}}^{-}$ to 0 results in transient instability. These findings verify the effectiveness of the regions R_{ABCD} and R_{knml} constructed in Fig. 16. Further analysis comparing experimental results with $\boldsymbol{I}_{\mathbf{t}}^{-} = 0$ and $\boldsymbol{I}_{\mathbf{t}}^{-} = 0.3 \angle 270°$ at point b_4 reveals that absorbing NS reactive current by the VSC can improve the PSTS of the system.

E. Visualization of FR-PNC in Negative-Sequence Current Space With Different Positive-Sequence Injection Currents

Fig. 18(a)–(d) shows the visualization boundaries of the FR-PNC in NS current space with $\alpha = 0.5$ and $\boldsymbol{I}_{\mathbf{t}}^{+}$ selected to be $0.4 \angle 0°$, $0.4 \angle 90°$, $0.25 \angle 180°$, and $0.25 \angle 270°$, corresponding to regions R_{opq}, R_{rstu}, R_{vxy}, and R_{YyzZ}, respectively. Moreover, the visualized boundary of the FR-PNC in NS current space with $\boldsymbol{I}_{\mathbf{t}}^{+} = \mathbf{0}$ is also given in Fig. 18 for comparison, corresponding to region R_{EFGH} (red dashed line).

By comparing the PSTS boundaries rs, ut, EF, and GH in Fig. 18(b), it can be concluded that during asymmetric faults, injecting PS reactive current by VSC can effectively enhance the PSTS of the system. Conversely, as observed in Fig. 18(a), (c), and (d), absorbing PS reactive current or absorbing/injecting active current by VSC can reduce the projection of FR-PNC in negative sequence current space, and deteriorate the PSTS of the system. The above results are summarized in Table III.

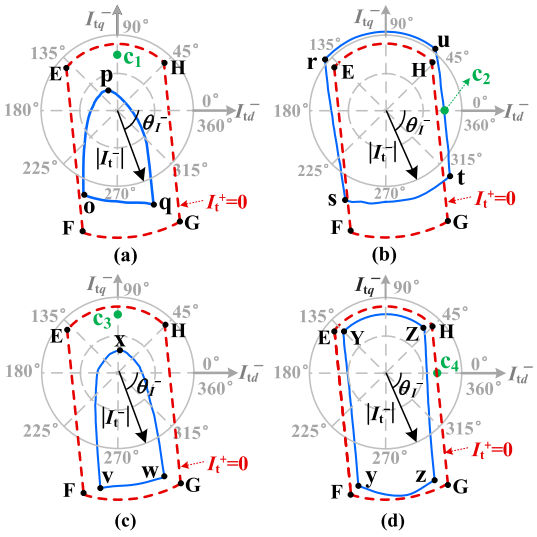

Fig. 18. Visualization of FR-PNC in NS injection current space. (a) $\boldsymbol{I_t^+} = 0.4 \angle 0°$ ($\boldsymbol{I_{td}^+} = 0.4$ pu). (b) $\boldsymbol{I_t^+} = 0.4 \angle 90°$ ($\boldsymbol{I_{tq}^+} = 0.4$ pu). (c) $\boldsymbol{I_t^+} = 0.25 \angle 180°$ ($\boldsymbol{I_{td}^+} = -0.25$ pu). (d) $\boldsymbol{I_t^+} = 0.25 \angle 270°$ ($\boldsymbol{I_{tq}^+} = -0.25$ pu).

TABLE III
EFFECT OF DIFFERENT PS INJECTION CURRENTS ON PSTS

$\boldsymbol{I_t^+}$	Characterization of PS injection current	Impact of PSTS
$0.4\angle 0°$	Injecting of PS active current	Deterioration
$0.4\angle 90°$	**Injecting of PS reactive current**	**Improvement**
$0.25\angle 180°$	Absorbing of PS active current	Deterioration
$0.25\angle 270°$	Absorbing of PS reactive current	Deterioration

The specific operating parameters (I_t^-, θ_I^-) of point c_2 were selected to be (0.38, 0°). From Fig. 18(b), c_2 is located outside the region R_{EFGH} and located on the boundary of R_{rstu}. Thus, PLL synchronization transient instability will occur with $\boldsymbol{I_t^+} = \boldsymbol{0}$. However, the transient instability can be avoided by increasing the PS reactive injection current of the VSC to 0.4 pu. The experimental results shown in Fig. 19(b) validate the above conclusion and indicate that the PSTS of the system can be improved by injecting PS reactive current.

For points c_1, c_3, and c_4 depicted in Fig. 18(a), (c), and (d), with operating parameters (I_t^-, θ_I^-) of (0.36, 90°), (0.42,90°), and (0.34, 0°), respectively. When $\boldsymbol{I_t^+} = \boldsymbol{0}$, it can be known that the points c1, c3, and c4 are all located in the region R_{EFGH}, corresponding to transient stability. However, in these scenarios, if $\boldsymbol{I_t^-}$ selected to be $0.4 \angle 0°$, $0.25 \angle 180°$, and $0.25 \angle 270°$ respectively, and c_1, c_3, and c_4 will be located outside the regions R_{opq}, R_{vxy}, and R_{YyzZ}, respectively, which corresponds PLL synchronization transient instability. The experimental results in Fig. 14(a), (c), and (d) for $\boldsymbol{I_t^+} = \boldsymbol{0}$ and $\boldsymbol{I_t^+} = 0.4 \angle 0°$, $0.25 \angle 180°$, and $0.25 \angle 270°$ support the deduction that absorbing PS reactive current or absorbing/injecting PS active current by VSC both degrade the PSTS of the system. Therefore, it is essential to carefully design the current injection strategy of VSC during asymmetric faults to improve the PSTS of the system.

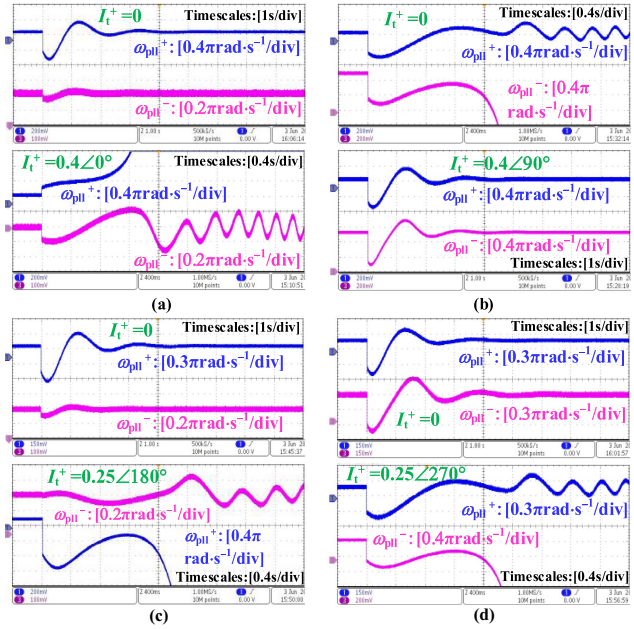

Fig. 19. Experimental results: (a) c_1. (b) c_2. (a) c_3. (a) c_4. (a) Point $\mathbf{c}_1(\boldsymbol{I_t^-} = 0.36 \angle 90°)$. (b) Point $\mathbf{c}_2(\boldsymbol{I_t^-} = 0.38 \angle 0°)$. (c) Point $\mathbf{c}_1(\boldsymbol{I_t^-} = 0.42 \angle 90°)$. (d) Point $\mathbf{c}_2(\boldsymbol{I_t^-} = 0.34 \angle 0°)$.

V. CONCLUSION

In this article, the LEDA of the WG-VSC under asymmetric fault conditions, considering the impact of PN sequence coupling, has been built based on the TS method. With the obtained LEDA, the FR-PNC considering PN sequence coupling is built with the perspective of ensuring PSTS during asymmetric faults. Then, an algorithm is proposed to visualize this 4-D FR-PNC in a 2-D subspace, providing a useful tool for current injection strategy design and PSTS analysis. Based on theoretical analysis and verified results, the main conclusions of this article can be summarized as follows.

1) The effect of PN sequence coupling on the PSTS of the system is negligible when the fault location is far from the PCC. However, when the fault location is close to the PCC, the PN sequence coupling has a significant effect on its PSTS, and ignoring PN sequence coupling may lead to inaccurate analysis results. The findings are valuable for understanding the effect of PN sequence coupling on the PSTS of the system.
2) Injecting NS reactive current by VSC can be an effective method to reduce the amplitude of the NS PCC voltage and alleviate the detrimental effects of voltage unbalance [29]. However, our research suggests that this practice also impairs the PSTS of the system during asymmetric faults. Therefore, a trade-off must be considered between the PSTS and the ability to suppress NS voltage when planning NS reactive current injection control strategies.

Regarding future work, the following aspects are suggested: 1) Developing a control method to improve the PSTS of the system under asymmetric faults. 2) Analyzing the PSTS of multiparalleled WG-VSCs during asymmetric grid faults.

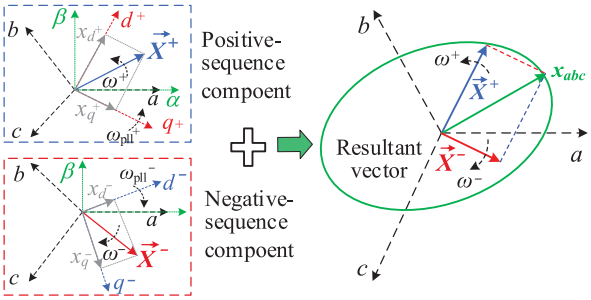

Fig. 20. Schematic diagram of $\vec{\boldsymbol{X}}^{+}$ and $\vec{\boldsymbol{X}}^{-}$.

TABLE IV
EXPRESSIONS OF $\mathbf{K_i}$

K_i	SLG	DLG	LL
K_1	$\frac{Z_g^- + Z_g^0 \,/\!/\, Z_L^0 + 3R_F}{Z_g^+ + Z_g^- + Z_g^0 \,/\!/\, Z_L^0 + 3R_F}$	$\frac{Z_g^0 \,/\!/\, Z_L^0 + 3R_F}{Z_g^+ + 2(Z_g^0 \,/\!/\, Z_L^0) + 6R_F}$	$\frac{Z_g^- + R_F}{Z_g^+ + Z_g^- + R_F}$
K_2	$\frac{-Z_g^-}{Z_g^+ + Z_g^- + Z_g^0 \,/\!/\, Z_L^0 + 3R_F}$	$\frac{Z_g^0 \,/\!/\, Z_L^0 + 3R_F}{Z_g^+ + 2(Z_g^0 \,/\!/\, Z_L^0) + 6R_F}$	$\frac{Z_g^-}{Z_g^+ + Z_g^- + R_F}$
K_3	$\frac{Z_g^+ + Z_g^0 \,/\!/\, Z_L^0 + 3R_F}{Z_g^+ + Z_g^- + Z_g^0 \,/\!/\, Z_L^0 + 3R_F}$	$\frac{Z_g^0 \,/\!/\, Z_L^0 + 3R_F}{Z_g^- + 2(Z_g^0 \,/\!/\, Z_L^0) + 6R_F}$	$\frac{Z_g^+ + R_F}{Z_g^+ + Z_g^- + R_F}$

TABLE V
SYSTEM PARAMETERS IN LOW-VOLTAGE-SIDE

System	Parameter name	Value
Base values	Base value of power	50 kW
	Base value of ac voltage	400 V
	Base value of frequency	50 Hz
hardware parameter	Switching frequency	10 kHz
	LC filter L_f/ C_f	0.1/0.04 pu
	X_L/R_L	0.5/0.05 pu
	X_g/R_g	0.4/0.04 pu
	Ground resistance R_F	4.5e-6 pu
	$I_{td,0}^{+}/I_{tq,0}^{+}/V_g$	0.9 pu/0.4 pu/1pu
	Maximum current I_m	1 pu
control parameter	PLL PI parameters k_p/k_i	10/50
	Gain of SOGI unit k_{SOGI}	1.414
	PR parameters $k_{pi}/k_{ri}/\omega_c$	1/10/6.5

APPENDIX A

A schematic diagram of $\vec{\boldsymbol{X}}^{+}$ and $\vec{\boldsymbol{X}}^{-}$ for the system under an asymmetrical fault is shown in Fig. 20.

APPENDIX B

The expressions of $\boldsymbol{K_i}$ for different fault types are shown in Table IV during asymmetric faults.

APPENDIX C

The SCR of the system is defined as

$$\mathrm{SCR} = 1\sqrt{(X_L + X_g)^2 + (R_L + R_g)^2}. \tag{C1}$$

From Table V, the SCR of the system in this article can be calculated to be 1.1. Ashabani and Mohamed [30] pointed out that a system with SCR > 3 could be considered a strong grid. When SCR < 3, the system is seen as a weak grid. Thus, the ac system considered in this article is indeed a weak grid.

APPENDIX D

The nonlinear dynamic model (5) for the WG-VSC system is first expressed as $\dot{\boldsymbol{x}} = \boldsymbol{A}(\boldsymbol{x})(\boldsymbol{x}\text{-}\mathbf{x_e})$, where $\boldsymbol{A}(\boldsymbol{x})$ is a nonlinear matrix function with state variables as elements. The specific expression of $\boldsymbol{A}(\boldsymbol{x})$ is shown in the following equation:

$$A(\boldsymbol{x}) = \begin{bmatrix} -k_p f_1(\delta^+, \delta^-) & -k_i & -k_p f_3(\delta^-) & 0 \\ f_1(\delta^+, \delta^-) & 0 & f_3(\delta^-) & 0 \\ -k_p f_4(\delta^+) & 0 & -k_p f_2(\delta^+, \delta^-) & -k_i \\ f_4(\delta^+) & 0 & f_2(\delta^+, \delta^-) & 0 \end{bmatrix} \tag{D1}$$

where the nonlinear functions f_1–f_4 are shown as follows:

$$f_1 = \begin{cases} g_1(\delta^+, \delta^-) & \delta^+ \neq \delta_e^+ \\ K_1 V_g^+ \cos(\delta_e^+ - \phi) + Z_c I_t^- \cos\varphi_1 & \delta^+ = \delta_e^+ \end{cases}$$

$$f_2 = \begin{cases} g_2(\delta^+, \delta^-) & \delta^- \neq \delta_e^- \\ K_2 V_g^+ \cos(\delta_e^- + \phi_4) + Z_c I_t^+ \cos\varphi_2 & \delta^- = \delta_e^- \end{cases}$$

$$f_3 = \begin{cases} Z_c I_t^- (\sin\varphi_1 + \sin(\delta^- - \delta_e^- - \varphi_1))/ \\ \quad (\delta^- - \delta_e^-) & \delta^- \neq \delta_e^- \\ Z_c I_t^- \cos(\delta_e^- + \delta_e^+ - \phi_c - \theta_I^-) & \delta^- = \delta_e^- \end{cases}$$

$$f_4 = \begin{cases} Z_c I_t^+ (\sin\varphi_2 + \sin(\delta^+ - \delta_e^+ - \varphi_2))/ \\ \quad (\delta^+ - \delta_e^+) & \delta^+ \neq \delta_e^+ \\ Z_c I_t^+ \cos(\delta_e^- + \delta_e^+ + \phi_c - \theta_I^+) & \delta^+ = \delta_e^+ \end{cases} \tag{D2}$$

where g_1 and g_2 are shown as

$$g_1 = \frac{(K_1 V_g^+ \sin(\delta_e^+ - \phi_1) + Z_c I_t^- \sin\varphi_1)(\cos(\delta^+ - \delta_e^+) - 1)}{\delta^+ - \delta_e^+} + \frac{(K_1 V_g^+ \cos(\delta_e^+ - \phi) + Z_c I_t^- \cos\varphi_1)\sin(\delta^+ - \delta_e^+)}{\delta^+ - \delta_e^+}$$

$$g_2 = \frac{(K_2 V_g^+ \sin(\delta_e^- + \phi_4) + Z_c I_t^+ \sin\varphi_2)(\cos(\delta^- - \delta_e^-) - 1)}{\delta^- - \delta_e^-} + \frac{(K_2 V_g^+ \cos(\delta_e^- + \phi_4) + Z_c I_t^+ \cos\varphi_2)\sin(\delta^- - \delta_e^-)}{\delta^- - \delta_e^-} \tag{D3}$$

where $\varphi_1 = \delta^- + \delta_e^+ - \phi_c - \theta_I^-$ and $\varphi_2 = \delta^+ + \delta_e^- + \phi_c - \theta_I^+$.

Each nonlinearity $f_r(\boldsymbol{x})$ in the matrix $\boldsymbol{A}(\boldsymbol{x})$ has a maximum $f_{r\max}$ and a minimum $f_{r\min}$ in the region $\psi = \{\boldsymbol{x} \in R^4 \,|\, x_{l\min} \leq x_l \leq x_{l\max}\}$, corresponding to the two IF-THEN rules. Thus, the TS fuzzy model of the system can be described by 2^4 IF-THEN rules. One of these rules, R^i ($i = 1, \ldots, 2^4$), is used as an example to demonstrate the IF-THEN rule as follows:

Rule R^i: If $f_1(\boldsymbol{x})$ is $f_{1\min}$, $f_2(\boldsymbol{x})$ is $f_{2\min}$, $f_3(\boldsymbol{x})$ is $f_{3\max}$, and $f_4(\boldsymbol{x})$ is $f_{4\max}$, the system can be described as the subsystem

$$\dot{\boldsymbol{x}} = \boldsymbol{A}_i(f_{1\min}, f_{2\min}, f_{3\max}, f_{4\max})(\boldsymbol{x} - \mathbf{x}_e). \tag{D4}$$

Based on the 2^4 IF-THEN rules, the TS fuzzy model of the system in region ψ can be expressed as follows:

$$\dot{\boldsymbol{x}} = \sum_{i=1}^{16} h_i(x_1, x_3)\boldsymbol{A}_i(\boldsymbol{x} - \mathbf{x}_e) \tag{D5}$$

TABLE VI
LEDA CONSTRUCTED USING DIFFERENT METHODS FOR $\mathbf{x_e}$,D1

Method	LMI method	SOS method	TS method
Runtimes	7505.5s	640.3s	2.13s
Volume of LEDA	2.794	2.294	1.545

TABLE VII
LEDA CONSTRUCTED USING DIFFERENT METHODS FOR $\mathbf{x_e}$,D2

Method	LMI method	SOS method	TS method
Runtimes	8041.5s	582.6s	1.19s
Volume of LEDA	0.882	0.644	0.29

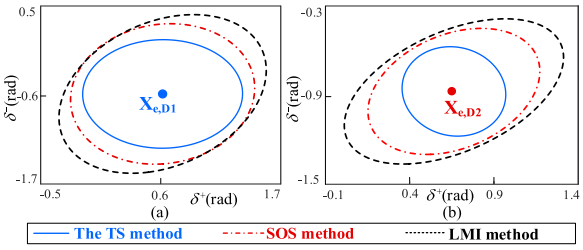

Fig. 21. Projections of LEDA constructed using different methods for $x_{e,D1}$ and (b) $x_{e,D2}$.

where the expressions of h_i is as follows:

$$h_i(x_1, x_3) = \Pi_{u=1}^{4} F_u^i(f_u) \Big/ \Sigma_{i=1}^{2^4} \Pi_{u=1}^{4} F_u^i(f_u) \tag{D6}$$

where $F_u^i(f_u)$ ($i = 1,2,\ldots,2^4$) denotes a fuzzy set or so-called membership function, which is defined in [31].

APPENDIX E

The comparison of runtimes and volumes of the LEDA constructed based on LMI, SOS, and TS methods has been provided here. Take the LEDA of $\mathbf{x_e}$,D1 and $\mathbf{x_e}$,D2 as an example. Tables VI and VII compare the runtimes and the volume of the LEDA constructed based on LMI, SOS, and TS methods for available EPs $\mathbf{x_e}$,D1 and $\mathbf{x_e}$,D2, respectively. On the $\delta^+ - \delta^-$ plane, Fig. 21(a) and (b) compares the projections of LEDA constructed using the different methods for $\mathbf{x_e}$,D1 and $\mathbf{x_e}$,D2, respectively. All code was run on a computer with a CPU of GHz and 16 GB RMA.

It can be visualized from Fig. 21(a) and (b) that compared with the TS method, the LEDA constructed by the LMI and SOS methods have lower conservation, and the LEDA constructed by the LMI method has the largest volume and the lowest conservation. However, it can be seen from Tables I and II that the runtimes for constructing the LEDA by the LMI method are several hundred times that of the TS method. Also, the runtimes for constructing the LEDA by the SOS method are much larger than that of the TS method. Considering the computational burden and conservativeness, the TS method is used to construct the LEDA in this article.

APPENDIX F

Taking δ^+, δ^-, $\Delta\omega_{\text{pll}}^+$, and $\Delta\omega_{\text{pll}}^-$ as state variables, the fourth-order model (11) can be transformed into the following

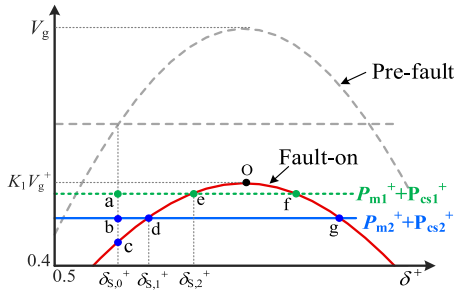

Fig. 22. Accelerating and maximum deceleration area diagram.

equation:

$$\begin{cases} J^+\ddot{\delta}^+ = P_{\text{m}}^+ + P_{\text{c}}^+(\delta^+,\delta^-) - P_{\text{e}}^+(\delta^+) - D^+(\delta^+,\delta^-)\dot{\delta}^+ \\ \qquad -D_{\text{c}}^+(\delta^+,\delta^-)\dot{\delta}^- \\ J^-\ddot{\delta}^- = P_{\text{m}}^- + P_{\text{c}}^-(\delta^+,\delta^-) - P_{\text{e}}^-(\delta^-) - D^-(\delta^+,\delta^-)\dot{\delta}^- \\ \qquad -D_{\text{c}}^-(\delta^+,\delta^-)\dot{\delta}^+ \end{cases} \tag{F1}$$

where P_{m}^+ and P_{m}^- represent the PS and NS mechanical power, respectively, P_{c}^+ and P_{c}^- represent the PS and NS sequence coupling mechanical power, P_{e}^+ and P_{e}^- are represented as PS and NS electromagnetic power, respectively, J^+ and J^- represent inertia coefficient related to PS and NS, respectively, with expressions $1/k_{\text{i}}$. D^+ and D^- represent PS and NS self-damping, respectively. D_{c}^+ and D_{c}^- represent PS and NS sequence coupling damping, respectively. The specific expression of the above variable is given in the following equation:

$$\begin{cases} P_{\text{ms}}^+ = Z_{\text{e}}^+ I_{\text{t}}^+ \sin(\phi_{\text{e}}^+ - \theta_I^+); P_{\text{e}}^+(\delta^+) = K_1 V_g^+ \sin(\delta^+ - \phi_1) \\ P_{\text{c}}^+(\delta^+,\delta^-) = Z_{\text{c}} I_{\text{t}}^- \sin(\phi_{\text{c}} + \theta_I^- - \delta^+ - \delta^-) \\ D^+(\delta^+,\delta^-) = \frac{k_{\text{p}}}{k_{\text{i}}}\left(K_1 V_g^+ \cos(\delta^+ - \phi_1)\right. \\ \qquad \left. + Z_{\text{c}} I_{\text{t}}^- \cos(\phi_{\text{c}} + \theta_I^- - \delta^+ - \delta^-)\right) \\ D_{\text{c}}^+(\delta^+,\delta^-) = \frac{k_{\text{p}}}{k_{\text{i}}} Z_{\text{c}} I_{\text{t}}^- \cos(\phi_{\text{c}} + \theta_I^- - \delta^+ - \delta^-) \\ P_{\text{m}}^- = Z_{\text{e}}^- I_{\text{t}}^- \sin(-\phi_e^- - \theta_I^-); P_{\text{e}}^-(\delta^-) = K_2 V_{\text{g}} \sin(\delta^- + \phi_2) \\ P_{\text{c}}^+(\delta^+,\delta^-) = Z_{\text{c}} I_{\text{t}}^+ \sin(-\phi_{\text{c}} + \theta_I^+ - \delta^+ - \delta^-) \\ D^-(\delta^+,\delta^-) = \frac{k_{\text{p}}}{k_{\text{i}}}\left(K_2 V_g^+ \cos(\delta^- + \phi_2)\right. \\ \qquad \left. + Z_{\text{c}} I_{\text{t}}^+ \cos(-\phi_{\text{c}} + \theta_I^+ - \delta^+ - \delta^-)\right) \\ D_{\text{c}}^-(\delta^+,\delta^-) = \frac{k_{\text{p}}}{k_{\text{i}}} Z_{\text{c}} I_{\text{t}}^+ \cos(-\phi_{\text{c}} + \theta_I^+ - \delta^+ - \delta^-) \end{cases} \tag{F2}$$

From the point of view of mechanism analysis, we temporarily ignore the effect of nonlinear self-damping and sequence coupling damping. In addition, for PS sequence coupling mechanical power P_{c}^+, which can be divided into static PS sequence coupling mechanical power P_{cs}^+ and dynamic PS sequence coupling mechanical power P_{cd}^+, as shown in the following equation:

$$\begin{cases} P_{\text{c}}^+(\delta^+,\delta^-) = P_{\text{cs}}^+ + P_{\text{cd}}^+(\delta^+,\delta^-) \\ P_{\text{cs}}^+(\delta^+,\delta^-) = Z_{\mathbf{c}} I_{\text{t}}^- \sin(\phi_{\text{c}} + \theta_I^- - \delta_{\text{e}}^+ - \delta_{\text{e}}^-) \end{cases} . \tag{F3}$$

Neglecting the influence of dynamic PS sequence coupling mechanical power P_{cd}^+, Fig. 22 compares the acceleration area and maximum deceleration area of Case 1 and the first transient process of Case 2. In Fig. 22, P_{m1}^+ and P_{cs1}^+ and P_{m2}^+andP_{cs2}^+ denote the PS mechanical power, static PS sequence coupling

mechanical power corresponding to Case 1, and the first transient process of Case 2, respectively. The acceleration area and maximum deceleration area corresponding to Case 1 and the first transient process of Case 2 are $S_{\rm cae}$ and $S_{\rm cbd}$ and $S_{\rm eof}$ and $S_{\rm dog}$, respectively.

It is obvious from Fig. 22 that compared with Case 1, the first transient process of Case 2 corresponds to a smaller static mechanical power, which corresponds to a smaller acceleration area and a larger maximum deceleration area. In the view of EAC, the transient stability of the system is improved under the first transient process of Case 2; this explains why $\Omega_V(\mathbf{x_e},_{\rm S1})$ is larger than $\Omega_V(\mathbf{x_e},_{\rm S2})$ from the physical mechanism aspect.

Note that the influence of nonlinear damping and dynamic sequence coupling mechanical power is not considered in the physical mechanism analysis, so the above analysis can only *qualitatively* analyze the transient stability of the system.

REFERENCES

[1] M. Farrokhabadi et al., "Microgrid stability definitions, analysis, and examples," *IEEE Trans. Power Syst.*, vol. 35, no. 1, pp. 13–29, Jan. 2020.

[2] M. G. Taul, X. Wang, P. Davari, and F. Blaabjerg, "An overview of assessment methods for synchronization stability of grid-connected converters under severe symmetrical grid faults," *IEEE Trans. Power Electron.*, vol. 34, no. 10, pp. 9655–9670, Oct. 2019.

[3] R. Ma, J. Li, J. Kurths, S. Cheng, and M. Zhan, "Generalized swing equation and transient synchronous stability with PLL-based VSC," *IEEE Trans. Energy Convers.*, vol. 37, no. 2, pp. 1428–1441, Jun. 2022.

[4] X. Fu et al., "Large-signal stability of grid-forming and grid-following controls in voltage source converter: A comparative study," *IEEE Trans. Power Electron.*, vol. 36, no. 7, pp. 7832–7840, Jul. 2021.

[5] B. Hu et al., "Synchronization stability enhancement of grid-following converter under inductive power grid," *IEEE Trans. Energy Convers.*, vol. 38, no. 2, pp. 1485–1488, Jun. 2023.

[6] H. Wu and X. Wang, "Design-oriented transient stability analysis of PLL-synchronized voltage-source converters," *IEEE Trans. Power Electron.*, vol. 35, no. 4, pp. 3573–3589, Apr. 2020.

[7] Q. Hu, L. Fu, F. Ma, and F. Ji, "Large signal synchronizing instability of PLL-based VSC connected to weak ac grid," *IEEE Trans. Power Syst.*, vol. 34, no. 4, pp. 3220–3229, Jul. 2019.

[8] Y. Zhang, C. Zhang, and X. Cai, "Large-signal grid-synchronization stability analysis of PLL-based VSCs using Lyapunov's direct method," *IEEE Trans. Power Syst.*, vol. 37, no. 1, pp. 788–791, Jan. 2022.

[9] Z. Zhang, R. Schuerhuber, L. Fickert, K. Friedl, G. Chen, and Y. Zhang, "Domain of attraction's estimation for grid connected converters with phase-locked loop," *IEEE Trans. Power Syst.*, vol. 37, no. 2, pp. 1351–1362, Mar. 2022.

[10] J. Chen, M. Liu, H. Geng, T. O'Donnell, and F. Milano, "Impact of PLL frequency limiter on synchronization stability of grid feeding converter," *IEEE Trans. Power Syst.*, vol. 37, no. 3, pp. 2487–2490, May 2022.

[11] Y. Li, Y. Tang, Y. Lu, F. Hua, and Z. Du, "Synchronization stability of grid-connected VSC with limits of PLL," *IEEE Trans. Power Syst.*, vol. 38, no. 4, pp. 3965–3976, Jul. 2023.

[12] J. Chen, M. Liu, T. O'Donnell, and F. Milano, "Impact of current transients on the synchronization stability assessment of grid-feeding converters," *IEEE Trans. Power Syst.*, vol. 35, no. 5, pp. 4131–4134, Sep. 2020.

[13] J. Pei, J. Yao, Y. Liu, S. Chen, P. Sun, and S. Huang, "Modeling and transient synchronization stability analysis for PLL-based renewable energy generator considering sequential switching schemes," *IEEE Trans. Power Electron.*, vol. 37, no. 2, pp. 2165–2179, Feb. 2022.

[14] X. Yi et al., "Transient synchronization stability analysis and enhancement of paralleled converters considering different current injection strategies," *IEEE Trans. Sustain. Energy*, vol. 13, no. 4, pp. 1957–1968, Oct. 2022.

[15] D. Pal and B. K. Panigrahi, "Reduced-order modeling and transient synchronization stability analysis of multiple heterogeneous grid-tied inverters," *IEEE Trans. Power Del.*, vol. 38, no. 2, pp. 1074–1085, Apr. 2023.

[16] J. Jia, G. Yang, and A. H. Nielsen, "A review on grid-connected converter control for short-circuit power provision under grid unbalanced faults," *IEEE Trans. Power Del.*, vol. 33, no. 2, pp. 649–661, Apr. 2018.

[17] Ö. Göksu et al., "Impact of wind power plant reactive current injection during asymmetrical grid faults," *IET Renewable Power Gener.*, vol. 7, no. 5, pp. 484–492, Sep. 2013.

[18] Y. Li, C. Lin, J. Hu, and J. Guo, "PLL synchronization stability of grid-connected VSCs under asymmetric ac faults," *IEEE Trans. Energy Convers.*, vol. 37, no. 4, pp. 2438–2448, Dec. 2022.

[19] H. Ahmed, Z. Tir, A. K. Verma, S. B. Elghali, and M. Benbouzid, "Quasi type-1 PLL with tunable phase detector for unbalanced and distorted three-phase grid," *IEEE Trans. Energy Convers.*, vol. 37, no. 2, pp. 1369–1378, Jun. 2022.

[20] X. Li, Z. Wang, L. Zhu, L. Guo, and C. Wang, "Analytical dual-sequence current injections feasible region of weak-grid connected VSC under asymmetric grid faults," *IEEE Trans. Power Syst.*, vol. 38, no. 6, pp. 5546–5559, Nov. 2023.

[21] M. G. Taul, S. Golestan, X. Wang, P. Davari, and F. Blaabjerg, "Modeling of converter synchronization stability under grid faults: The general case," *IEEE J. Emerg. Sel. Topics Power Electron.*, vol. 10, no. 3, pp. 2790–2804, Jun. 2022.

[22] P. Hackl, Z. Zhang, and R. Schuerhuber, "Unsymmetrical fault behavior of PLL based grid-connected converters," in *Proc. 24th Eur. Conf. Power Electron. Appl.*, 2022, pp. 1–10.

[23] X. He, C. He, S. Pan, H. Geng, and F. Liu, "Synchronization instability of inverter-based generation during asymmetrical grid faults," *IEEE Trans. Power Syst.*, vol. 37, no. 2, pp. 1018–1031, Mar. 2022.

[24] R. Liu, J. Yao, P. Sun, J. Pei, H. Zhang, and Y. Zhao, "Complex impedance-based frequency coupling characteristics analysis of DFIG-based WT during asymmetric grid faults," *IEEE Trans. Ind. Electron.*, vol. 68, no. 9, pp. 8274–8288, Sep. 2021.

[25] A. Akhavan, S. Golestan, J. C. Vasquez, and J. M. Guerrero, "Control and stability analysis of current-controlled grid-connected inverters in asymmetrical grids," *IEEE Trans. Power Electron.*, vol. 37, no. 12, pp. 14252–14264, Dec. 2022.

[26] S. Golestan, J. M. Guerrero, and J. C. Vasquez, "Three-phase PLLs: A review of recent advances," *IEEE Trans. Power Electron.*, vol. 32, no. 3, pp. 1894–1907, Mar. 2017.

[27] X. Li et al., " The largest estimated domain of attraction and its applications for transient stability analysis of PLL synchronization in weak-grid-connected VSCs," *IEEE Trans. Power Syst.*, vol. 38, no. 5, pp. 4107–4121, Sep. 2023.

[28] C. Zhang et al., "Synchronizing stability analysis and region of attraction estimation of grid-feeding VSCs using sum-of-squares programming," *Frontier Energy Res.*, vol. 8, 2020, Art. no. 56.

[29] S. Mortazavian and Y. A.-R. I. Mohamed, "Analysis and augmented model-based control design of distributed generation converters with a flexible grid-support controller," *IEEE Trans. Power Electron.*, vol. 34, no. 7, pp. 6369–6387, Jul. 2019.

[30] M. Ashabani and Y. A. I. Mohamed, "Integrating VSCs to weak grids by nonlinear power damping controller with self-synchronization capability," *IEEE Trans. Power Syst.*, vol. 29, no. 2, pp. 805–814, Mar. 2014.

[31] D. Marx, P. Magne, B. Nahid-Mobarakeh, S. Pierfederici, and B. Davat, "Large signal stability analysis tools in DC power systems with constant power loads and variable power loads—A review," *IEEE Trans. Power Electron.*, vol. 27, no. 4, pp. 1773–1787, Apr. 2012.

Zhi Wang received the B.Sc. and M.Sc. degrees in electrical engineering, in 2020 and 2023, respectively, from Tianjin University, Tianjin, China, where he is currently working toward the Ph.D. degree in electrical engineering.

His research interests include modeling, stability analysis, and control of power electronics-dominated power systems.

Li Guo (Member, IEEE) received the B.Sc. and the Ph.D. degrees in electrical engineering from South China University of Technology, Guangzhou, China, in 2002 and 2007, respectively.

He is currently a Full Professor with Tianjin University, Tianjin, China. His research interests include the optimal planning and design of microgrids, the coordinated operating strategy of microgrids, and advanced energy management systems.

Xialin Li (Member, IEEE) received the B.Sc. and Ph.D. degrees in electrical engineering from Tianjin University, Tianjin, China, in 2009 and 2014, respectively.

In 2016, under the State Scholarship Fund, he was invited as a Visiting Professor to the Department of Electrical and Computer Engineering, University of Alberta, Edmonton, AB, Canada. Since 2018, he has been an Associate Professor with the School of Electrical Engineering and Automation, Tianjin University. His research interests include the modeling and control of power converters, distributed generation, hybrid ac–dc microgrids, and multiterminal dc grids.

Xiulan Pang received the B.Sc. degree in electrical engineering from China Three Gorges University, Hubei, China, in 1988.

She is currently a Professorate Senior Engineer with SPIC Qinghai Photovoltaic Industry Innovation Center, Xining, China. She has participated in and presided over the construction of more than 20 hydropower stations, more than 10 wind power stations, and nearly 40 photovoltaic power stations, including several key projects such as the Qingyu dc ultra-high voltage (UHV) supporting power photovoltaic project, the national photovoltaic energy storage empirical experimental base, and the first batch of national Shage desert base. Her research interests include new energy power generation.

Xiaofeng Li received the B.Sc. degree in electrical engineering from North China Electric Power University, Beijing, China, in 1998.

He is currently a Senior Engineer with SPIC Qinghai Photovoltaic Industry Innovation Center, Xining, China. He has been responsible for and presided more than 40 photovoltaic power stations including supporting energy storage planning and design, such as the Qingyu dc UHV supporting power supply photovoltaic project, the national photovoltaic energy storage demonstration experimental base, and many other major projects. His research interests include new energy power generation.

Xu Zhou received the B.Sc. and M.Sc. degrees in electrical engineering from North China University of Technology, Beijing, China, in 2019 and 2022, respectively. He is currently working toward the Ph.D. degree with the School of Electrical and Information Engineering, Tianjin University, Tianjin, China.

His research interests include modeling, control, and stability analysis of the grid-forming converters and grid-following converters.

Chengshan Wang (Senior Member, IEEE) received the B.Sc., M.Sc., and the Ph.D. degrees in electrical engineering from Tianjin University, Tianjin, China, in 1983, 1985, and 1991, respectively.

From 1994 to 1996, he was a Visiting Scientist with Cornell University, Ithaca, NY, USA. In 1996, he was a Full Professor with Tianjin University. From 2001 to 2002, he was a Visiting Professor with Carnegie Mellon University, Pittsburgh, PA, USA. From 2009 to 2013, he was the Chief Scientist of the 973 project research on the Key Issues of Distributed Generation Systems that was participated by Chinese power engineering scientists from eight leading institutions. His research interests include the area of distribution system analysis and planning, distributed generation systems and microgrids, and power system security analysis.

Dr. Wang was the recipient of the Fok Ying Tung Fund, the Excellent Young Teacher Fund of Education Ministry, and a winner of the National Science Fund for Distinguished Young Scholars.